IRANIAN JOURNAL OF CATALYSIS

IJC
Iranian Journal of Catalysis

Recent Progress in Visible-Light Active (VLA) TiO₂ Nano-Structures for Enhanced Photocatalytic Activity (PCA) and Antibacterial Properties: A Review

Kasun L. Seneviratne[a], *Imalka Munaweera*[b,d*], *Sriyani E. Peiris*[a], *Colin N. Peiris*[a], *Nilwala Kottegoda*[b,c]

a) *Faculty of Humanities and Sciences, Sri Lanka Institute of Information Technology (SLIIT), New Kandy Road, Malabe, Sri Lanka*
b) *Department of Chemistry, Faculty of Applied Science, University of Sri Jayewardenepura, Gangodawila, Nugegoda, Sri Lanka*
c) *Center for Advanced Materials Research (CAMR), Faculty of Applied Sciences, University of Sri Jayewardenepura, Gangodawila, Nugegoda, Sri Lanka*
d) *Instrument Center, Faculty of Applied Sciences, University of Sri Jayewardenepura, Gangodawila, Nugegoda, Sri Lanka*

ABSTRACT

The applications of photocatalytic nanomaterial technology received intense scientific focus with the advent of nanotechnology. Applications based on TiO₂ nanoparticles have shown promise of photocatalytic efficiency among many semiconductor metal oxides. Titanium dioxide is utilized in many practical applications such as water and air purification, self-cleaning of surfaces, and energy production. The major drawback with TiO₂ based photocatalysts is the wide band gap, which requires UV light to produce the electron-hole pairs. This review article focus on techniques/methods to eliminate band gap which reduces photocatalytic efficiency. Application of semiconductor photocatalytic techniques to degrade organic pollutants and their antimicrobial activity is discussed here using model systems. Synthetic and natural nanohybrids are available today and have varying characteristics as options. Recently developed natural mineral based nanohybrids is the new trend in photocatalytic applications. It appears that the removal efficiency of existed photocatalysts is higher than that of synthetic products. Natural nanohybrids carry the advantages of low costs, avoiding extensive synthesizing conditions in future photocatalytic applications.

Keywords: Antibacterial activity; Metal doped TiO₂; Natural and synthetic based TiO₂ nanohybrids; Semiconductor nanomaterial; Visible active photocatalyst.

1. Introduction

The word "nano" has rapidly penetrated the public consciousness over the past decades. It has also sparked speculation of a seismic shift in most research and engineering fields [1]. Nanotechnology is a superior method of producing materials. It provides more for less, namely smaller, cheaper, lighter and faster devices with improved functionality, utilizing less material and consuming less energy [2]. Nanotechnology is essentially defined by a unit of scale, the nanometer, with powerful influence on the framework of matter. A nanometer (nm) is one-billionth of a meter or 100,000 times smaller than the wavelength of visible light (VL) [3].

*Corresponding author:
E-mail address: imalka@sjp.ac.lk (**I. Munaweera**)

A nanometer could be comprehended as the size of 10 hydrogen atoms or five silicon atoms in a line [4]. At the nanoscale, most material properties meet the properties of the atomic and molecular levels, such as wave-particle duality and quantum effects [5]. Nanoscale is also characterized by a notable increase in the ratio of surface area to volume, changing the physical properties of materials compared to macroscopic structures [6].

Nanotechnology can be successfully applied to create novel multifunctional materials [3,5]. Among the many applications, nano-functional hybrid materials have been investigated for environmental pollution control, specifically to decontaminate water pollutants at low-cost and slow release nitrogen fertilizer in agriculture [7–13]. Nanotechnology is findings its importance as medicinal and drug delivery agents [14–17], in food technology [18] and in rubber industry [9,19].

Fujishima and Honda discovered the photocatalytic activity in the 1970s, which led to a revolution in wastewater purification [20–22]. Carey *et al*. pioneered semiconducting material to dissociate organic pollutant "polychlorobiphenyl" [21,23]. Semiconductors possess the potential to degrade organic pollutants into carbon dioxide and water by absorbing photons [24,25]. Photocatalysis exposure of materials to ultra violet (UV), visible or near-infrared light induces photo-excitation. The photo-catalytic redox mechanism imitated by photo excitation inactivate a broad spectrum of bacteria and organic pollutants [26]. The electrons (e^-) in the semiconductor's valence band (VB) are energized to the conduction band (CB), resulting in holes (h^+) in the VB. Redox reactions are initiated by the e^- and h^+ created in this process [3,26]. Various semiconductor materials like metal oxides (TiO_2, ZnO, SnO_2, Fe_2O_3, Al_2O_3, NiO, Nb_2O_5, ZrO_2, WO_3) [27–34], metal sulfides (PbS, CdS, ZnS, NiS) [35–43] and several other molecules capable of serving as photocatalysts are described [44–47]. The effectiveness of any semiconductor material would depend on lowest electron-hole recombination rate and capability of radical formation [48–50]. The photocatalytic activities need to be low-cost, eco-friendly, chemically inactive, photostable and long-lasting [13,20,25,51,52]. A semiconductor material can be synthesized in to nano-size, creating exceptional characters like large surface area, porosity, higher crystallinity, increased light absorption, efficient charge separation and high photostability. These properties enable achieving superior catalytic performances [24,26]. Photocatalytic efficiency of many nanomaterials, such as quantum dots (QDs), has been studied over the past decade. **Fig. 1** depicts the band gap (BG) positions against normal hydrogen electrode (NHE) in various semiconductor materials. According to the **Fig. 1**, the highest BG is attributed to Ta_2O_5 and SnO_2, suggesting restricted photon absorption from VL. Although BG of TiO_2 (anatase and rutile) is fairly close to ZnO, chemical instability is the disadvantage of ZnO as a semiconductor [53]. The TiO_2 is prominent as the common semiconductor material for photocatalysis [25,51,52,54].

TiO_2 is a n-type semiconductor which has many applications compared to other semiconductors [6,56–58]. A variety of photocatalysts have been developed using TiO_2 for crucial remediation in addressing many pollution-related environmental problems. More diverse photocatalysts are now synthesized by modifying TiO_2 structure for improved efficiency [30, 31,58–77]. However, TiO_2 photocatalyst possess the disadvantages of extended BG, poor sorption capability, minimum surface area, poor sunlight absorption (<5%), frequent recombination of electron–hole pairs (e^--h^+) and complexity in removing it from liquids, hence TiO_2 brings in limitations in photocatalytic efficiency [13,20,22,28,42].

The photocatalytic activity (PCA) of semiconductors, including TiO_2 could improve strategies like changing the morphology, crystallinity of phase, defect sites, pore size, and reducing the particle size [26]. The morphology of a crystal plays a major role in PCA. Scientists have synthesized nanotubes [78], nanowires [75,79], nanorods [52,80], nanoflowers, 1-Dimensional nanostructures [81], popcorn [82], and core-shell structure [83] changing the morphology of TiO_2. TiO_2 has three major polymorphs, namely, anatase, rutile, and brookite. Brookite is orthorhombic in shape, while anatase and rutile are of tetragonal shapes [84]. Anatase possess greater photocatalytic performance due to its smaller particle size, lighter effective mass, and longer lifespan of photoexcited electrons and holes [85]. Anatase has indirect BG of 3.2 eV but rutile has direct BG is 3.0 eV and brookite has direct BG of 3.4 eV [50,54,56,85,86]. As a result, anatase and brookite only activates in the UV region in solar spectrum. Rutile, on the other hand, get activated by absorbing VL photons. In contrast to anatase and brookite, rutile is thermodynamically stable. Rutile is formed by the irreversible and exothermic conversion of anatase/brookite TiO_2 over 600 °C [50,87]. Even though rutile is visible light active (VLA), its higher recombination rate, formation difficulties, and poor reduction potential in CB, make it poor photocatalyst out of three polymorphs [86]. The mixed phase of anatase and rutile is more effective photocatalysts than pristine TiO_2 [22,54,87]. Brookite synthesis is considerably hard to achieve in normal conditions [88]. Brookite is a better photocatalyst than rutile because electrons are held at reasonable depths, thus allowing both e^--h^+ to be available for reduction and oxidation reactions [85,87,89,90]. According to recent publications, electron transfer reactions may also occur in brookite based composites, which gives highly efficient PCA [88]. Numerous techniques were used to extend the BG of TiO_2 to the VL region, including doping, development of heterojunctions, morphological tailoring, oxygen vacancy generation and surface modification [91–94]. More unique VLA photocatalytic materials and methods have been recently developed to eliminate microorganisms and organic pollutants from wastewater [26,92].

A photocatalyst must answer the following three questi-
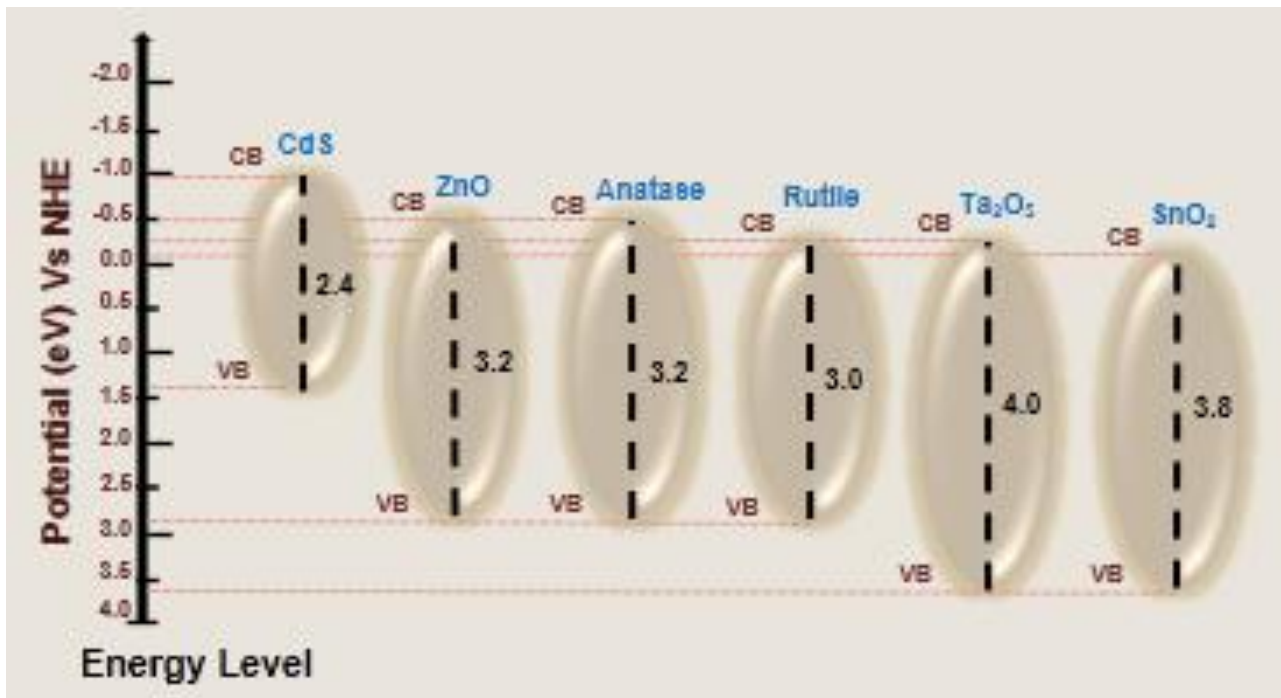
Fig. 1. Band Gap Positions of Semiconductor Materials Against Normal Hydrogen Electrode (NHE) [55].

-ons for excellence (1) Achieving higher reactivity against organic contaminants in using solar energy, (2) Eliminating high recombination rates and achieving perfect e^--h^+ separation and (3) Ability for industrial application [91]. This current review paper attempts to highlight findings of the last ten years focused on VLA TiO_2 nanohybrids and their application to PCA and antibacterial properties. In this paper, we present VLA TiO_2 synthesis routes (synthetic and natural) and characterization strategies that can be applied to classify nanomaterials. There is no literature on natural minerals pathway to synthesize VLA nanomaterials. We summarize the pollutant reduction efficiency of synthetic VLA TiO_2 nanomaterials. Finally, we discuss the recently synthesized natural mineral based VLA TiO_2 nanohybrids and their use as photocatalysts in numerous applications. There is room to identify critical points in natural and synthetic photocatalysts and their productivity for elimination of environmental pollutants. Thus, this review articled examines different photocatalysts and their synthesis aiming at industrial applications. This review also helps in recognizing more eco-friendly photocatalytic technology.

2. Theory of Photocatalysis

The primary source of the nanotechnological treatment method is the photocatalyst. As a result, several photocatalysts have been identified as potential materials for wastewater treatment [37,38,95]. The photocatalytic process begins by absorbing photons from the UV and VL equal to or greater than the BG energy. The e^--h^+ pair occurs when an electron in VB migrates to CB, resulting in the formation of a hole in VB. The e^--h^+ pair migrate to the surface of the semiconductor, where reduction and oxidation reactions occur at the adsorbed pollutant. Two radical species, hydroxyl (OH$^•$) and superoxide ($O_2^{•-}$) were formed through surface chemical reactions in the semiconductor. Generated $O_2^{•-}$ radical reacts with H^+ to form hydroperoxyl radical (HO$^•_2$) and finally convert into H_2O_2. H_2O_2 is also generated *via* the direct two-electron reduction in O_2 [96]. The e^--h^+ will rejoin by releasing photons and heat into the outer environment causing deactivation of the semiconductor [97]. This activation and deactivation process continuously occurs in rapid time intervals [50]. **Fig. 2** depicts the five steps in all heterogeneous photocatalysis process: transportation of pollutant, adsorption to catalyst surface, disintegrating reactions, desorption of by products and by-products release into liquid phase, respectively. The pollutant must be adsorbed into catalyst surface to initiate the dissociation reactions. During dissociation utilizing energized radicals, organic molecules in the waste material will break down into by products [92].

All advanced oxidation process (AOP) generating radicals (OH$^•$, Cl$^•$, Cl$_2^•$, ClO$^•$, HClO$^•$, F$^•$, Br$^•$) can decompose organic compounds into CO_2, H_2O and inorganic salts [98–100]. In oxidizing organic molecules, OH$^•$ (2.80 eV) radicals perform better than
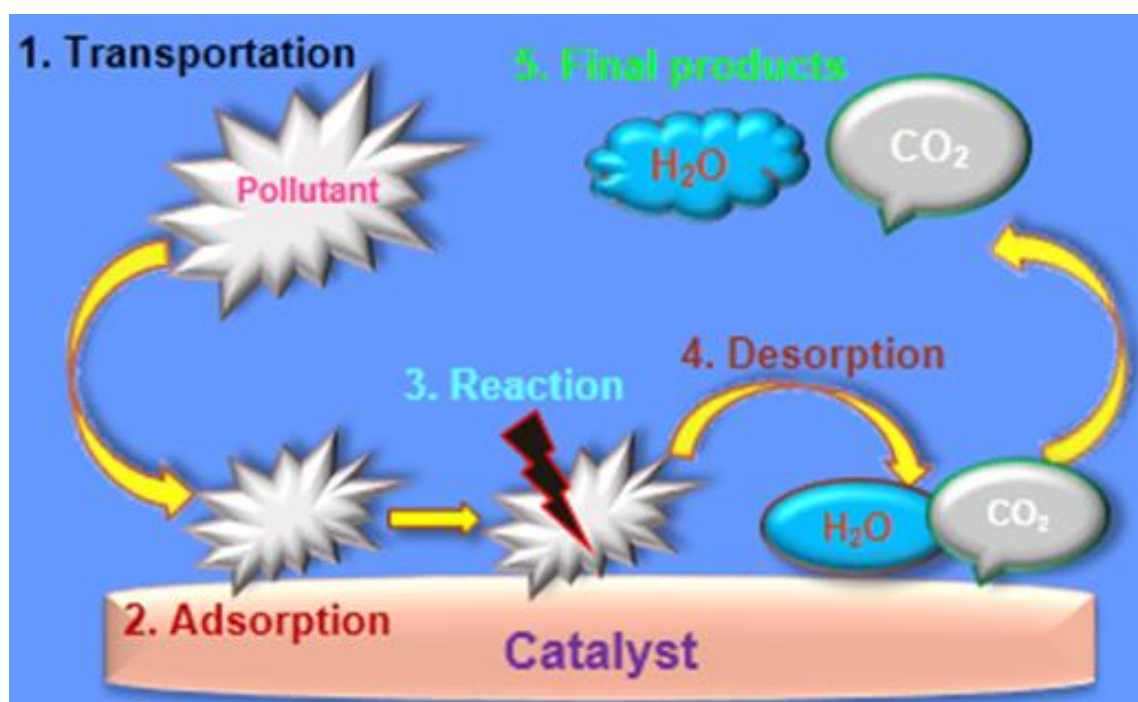
Fig. 2. Five Steps in Heterogeneous Photocatalysis Process [92].

H_2O_2 (1.78 eV) and O_3 (2.07 eV) [87,101]. Due to the radical participation, AOPs brings in excellent thermodynamic and kinetic reaction efficiency. In addition, $HO^{\bullet}$ enhances the reaction 10^6–10^{12} fold faster than other oxidants, such as O_3. $HO^{\bullet}$ is the second most energetic oxidant after fluorine radical. The reaction rate constant of $HO^{\bullet}$ involved in reactions are several times higher than O_3 [101].

Two simultaneous processes, oxidation and reduction, occur on a semiconductor surface with adsorbed pollutants, oxidation occurs due to photogenerated holes on the VB and reduction happens due to photogenerated electrons [102]. An important benefit of TiO_2 over other semiconductors is its use to reduce protons (E_{NHE} (H^+/H_2) = 0.0 eV) and oxidize water (E_{NHE} (O_2/H_2O) = 1.23 eV) concurrently [103]. Moreover, $E°$ (O_2/H_2O) = 1.23 eV for the donor species adsorbed on the TiO_2 photocatalyst is more negative than potential of TiO_2 VB (V/E_{NHE}= +2.5 at pH=7), whereas, $E°$ ($O_2/O_2°$) = -0.33 eV for acceptor molecules is more positive than potential of TiO_2 VB (-0.52 eV/E_{NHE} at pH=7) [103].

3. Photocatalytic Mechanism of TiO₂ Based Photocatalyst

The photocatalytic mechanism explains how organic molecules are degraded or oxidized by reactive oxygen species (ROS). The semiconductor surface determines whether the degradation reaction is partial or complete for attached pollutant molecules. Therefore, expanding the oxidation surface area of the nanohybrid is an essential feature in the synthesis method. Increased number of pollutant molecules bound to the accessible surface at nanohybrids, makes a reaction quick. Recent publications describe photocatalytic degradation processes for various organic pollutants [35,36,40,41,44,104–107]. The reaction 1-7 and **Fig. 3** depicts the general mechanism of semiconductor photocatalysis using solar light [108,109]. After absorbing photons from sunlight, electron (e^-) get excited to CB and created hole (h^+) at VB. The e^- will reduce molecular O_2 and generate ROS. Also, positive charged h^+ oxidize water molecules to generate ROS. The generated ROS break down the pollutant into CO_2 and H_2O.

$$\text{Semiconductor} + h\upsilon \rightarrow e_{cb}^- + h_{vb}^+ \qquad (1)$$

$$e_{cb}^- + h_{vb}^+ \rightarrow \text{Energy} \qquad (2)$$

$$h_{vb}^+ + \text{Pollutant} \rightarrow \text{Pollutant}^+ \qquad (3)$$

$$h_{vb}^+ + H_2O \rightarrow OH^{\cdot} + H^+ \qquad (4)$$

$$h_{vb}^+ + HO^- \rightarrow OH^{\cdot} \qquad (5)$$

$$e_{cb}^- + O_2 \rightarrow O_2^{\cdot -} \qquad (6)$$

$$\text{ROS} + \text{Pollutant} \rightarrow CO_2 + H_2O \qquad (7)$$
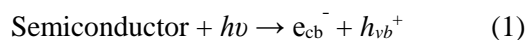
Dye-sensitized photo-degradation technique brings in few variations, as shown in the reactions 8-15 below. Photodegradation starts by collecting photons from dye molecules which get excited. Then it transfers electrons to anatase CB. As a result, exciting e- reacts with adsorbed oxygen molecules and generates ROS species.
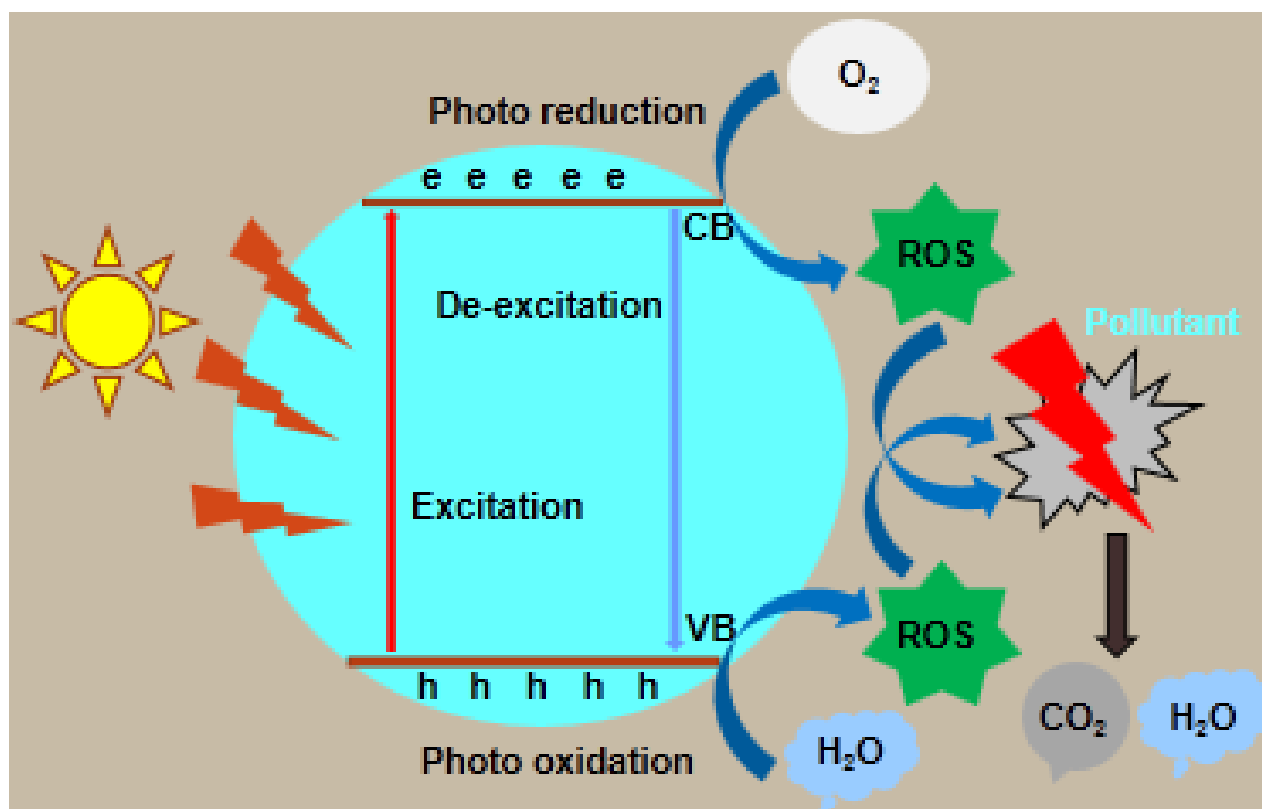
Fig. 3. Mechanism of Photocatalytic Activity of Heterogeneous Catalyst [92].

This is shown in a model pollutant humic acid using the dye-sensitized technique in reaction 8-15 [110]. Dye molecules get excited after absorbing a photon, or dye molecules are adsorbed into semiconductor surfaces (reaction 8-9). The attached dye molecules get excited by absorbing a photon and then undergo oxidation (reactions 10-11). Reaction 12-13 shows oxidation and reduction reactions of the surface-bound dye molecule. Reaction 14 indicates the reduction of the O_2 molecule. The energized dye molecule can also get be self-oxidized to donate e^- to CB (reaction 15).

$$Dye + h\upsilon \leftrightarrow Dye^* \qquad (8)$$

$$Semiconductor + Dye \leftrightarrow Dye\text{-}Semiconductor \qquad (9)$$

$$Dye\text{-}Semiconductor + h\upsilon \rightarrow Dye^*\text{-}Semiconductor \qquad (10)$$

$$Dye^* + Semiconductor \rightarrow Dye_{ox} + Semiconductor (e_{cb}^-) \qquad (11)$$

$$Dye^*\text{-}Semiconductor \rightarrow Dye_{ox}\text{-}Semiconductor (e_{cb}^-) \qquad (12)$$

$$Dye_{ox}\text{-}Semiconductor (e_{cb}^-) \rightarrow Dye\text{-}Semiconductor \qquad (13)$$

$$Dye_{ox}\text{-}Semiconductor (e_{cb}^-) + O_2 \rightarrow Dye_{ox}\text{-}Semiconductor + O_2^- \qquad (14)$$

$$Dye^* \rightarrow Dye_{ox} + (e_{cb}^-) \qquad (15)$$
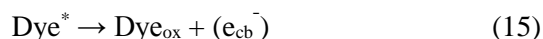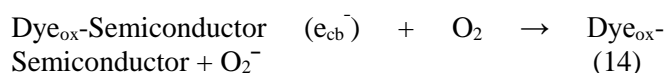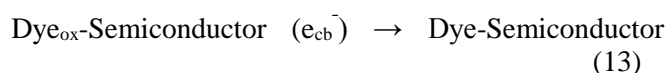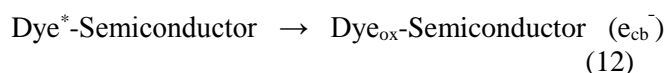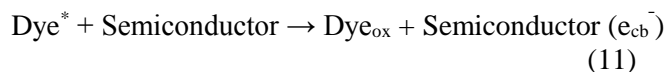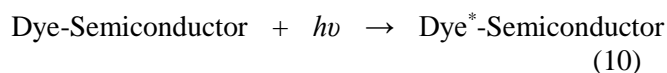
The photocatalytic action depends on several factors including, photocatalyst type, light intensity, pollutant concentration, catalyst concentration, pH of the solution, doping element *etc*, [47,92]. The photocatalytic reaction of semiconductors can be improved by optimizing the above factors, to increase speed of degradation and removal efficiency [53,108,111–113]. Following examples are evidence of improved heterogeneous nanohybrid's photocatalytic activity against model pollutants.

Fig. 4 shows the photodegradation reaction mechanism of methylene blue (MB) dissociation using TiO_2 nanomaterial [114,115]. A 90% photocatalytic efficiency was achieved using 10 nm TiO_2 nanoparticles, suggesting nanoparticle size reduction enhances the removal efficiency [53]. The reaction mechanism demonstrates that the degradation of MB starts with removing four methyl groups attached to N in the structure. The $-NH_2$ groups are then separated from both aromatic rings, followed by disintegration of the rings. The benzene ring eventually deteriorates into CO_2 and water. As a result, byproducts like NO_2 and SO_2 were also generated [53]. The VL active N-TiO_2 catalyst gave 88% of removal efficiency with a higher dissociation rate constant (1.2×10^{-2} min^{-1}). This illustrat-
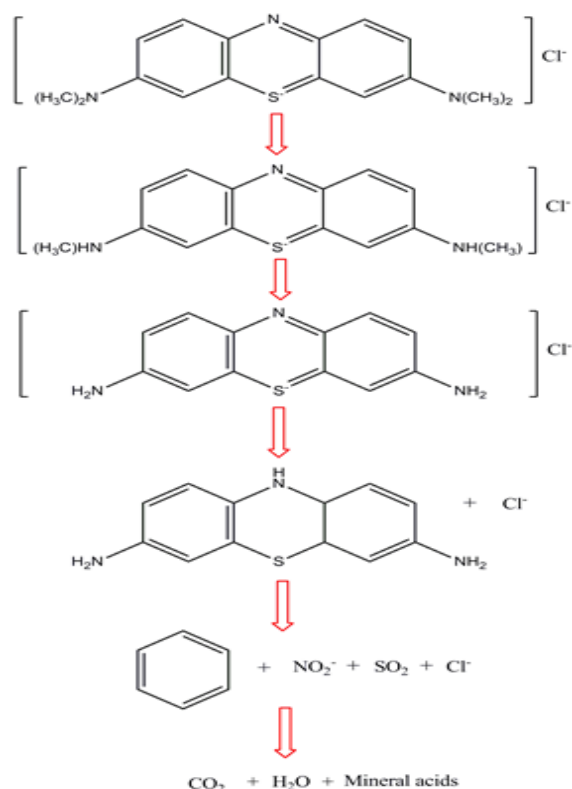
Fig. 4. The Photodegradation Mechanism of MB using TiO_2 Nanoparticle [53,114].

-es that doping element is another factor for enhancing photodegradation capability of the catalyst. Whereas pure TiO_2 gave only 60% removal efficiency , 40% of MB remains in the liquid phase showing doped TiO_2 is more efficient than pristine TiO_2 [108]. Another dye molecule, Methyl Orange is also used against AgBr/g-C_3N_4 catalyst, which gave ~80% degradation efficiency [116,117].

Lipid molecule degradation using S-TiO_2 nanoparticles serving as the VLA photocatalyst is shown in **Fig. 5**. The ROS species (ROO·) was formed by reacting O_2 with the olefinic H atom of the lipid molecule, resulting in a double conjugated molecule. Since the conjugated molecule was rearranged, it gets oxidized into a hydroperoxide molecule by reacting O_2 molecular. The hydroperoxide molecule is then converted into a peroxide molecule, followed by formation of ketones, aldehydes, acids, and CO_2 [118].

The photodegradation of phenol molecule using a Fe doped TiO_2 photocatalyst is shown in **Fig. 6**. Initially ROS (·OH) attack the phenolic ring, resulting in the formation of catechol (CT), hydroquinone (HQ), and benzoquinone (BQ). Decomposition of HQ and BQ results in development of benzenetriol (BT), hydrobenzoquinone (HBQ) and CT, which disintegrates into pyrogallol (PG), followed by carboxylic acid and finally, CO_2 and H_2O. Utilizing Fe-TiO_2 photocatalyst
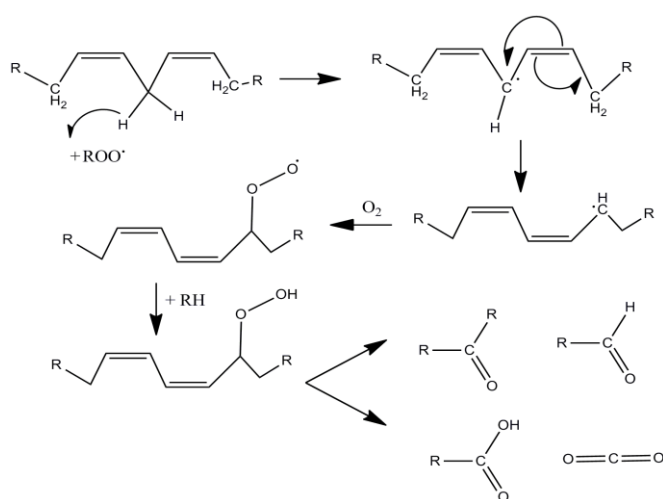
Fig. 5. Photodegradation Mechanism of Lipid Molecule using S-TiO_2 Nanohybrid [118].
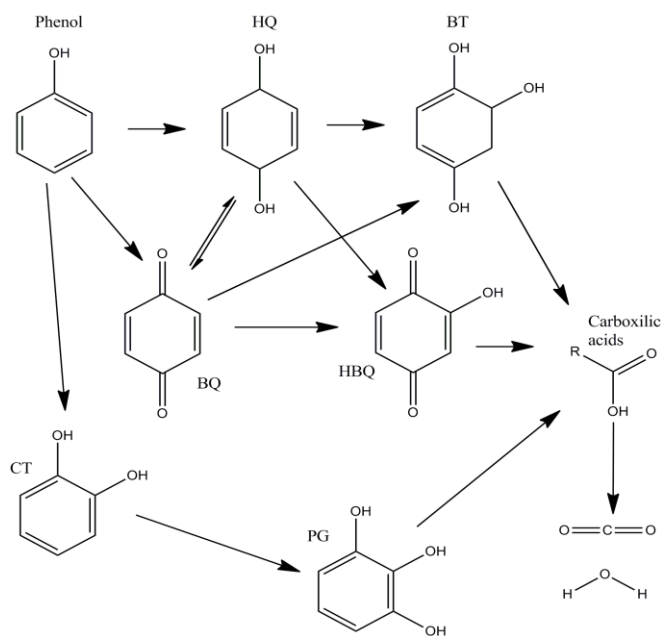
Fig. 6. The Mechanism of Phenol Degradation by using Fe-TiO_2 Nanomaterial [119].

40% of phenol degrade was achieved [119]. Choi *et al*. showed Pt(IV) doped TiO_2 was more effective than pristine TiO_2 by obtaining ~90% degradation within 2 hours with VL irradiation [120].

More photocatalytic applications against various organic pollutants are shown in **Table 1**. According to **Table 1** more heterogeneous photocatalysts were used. Recent publications reported their degradation efficiency against wastewater treatment. Many oxides, sulfides, phosphates *etc*, serving as heterogeneous photocatalysts were able to eliminate a substantial number of pollutants by coupling multi-elemental complexes, generating promising nanohybrids for future wastewater treatments.

Table 1. Heterogeneous Photocatalysts Utilized in Various Environmental applications

Photocatalyst	Pollutant	Efficiency	Reference
Se-TiO$_2$	RhB	91.3%	[76]
TiO$_2$/ZnO/GO	MO	57.7%	[13]
Fe$_2$O$_3$/TiO$_2$	MO	61.5%	[121]
	CR	46.8%	
Ag-TiO$_2$	E102	40.0%	[122]
α-Fe$_2$O$_3$/Cu$_2$O	MB	81.0%	[123]
CuO-nano-clinoptilolite	MB and BPB	61% and 32%	[28]
Co-NiAl$_2$O$_4$	MG	~45%	[33]
InVO$_4$-TiO$_2$	DR 23	95%	[61]
Ag/TiO$_2$	RB 255	94.46%	[62]
CuFe$_2$O$_4$	AR 206	~100%	[124]
Nb$_2$O$_5$	CR and MB	90% and 87%	[125]
CdS−Ag$_3$PO$_4$	MB	~90%	[107]
Co$_3$O$_4$	MO	76%	[126]
Mg-Al Oxide	Phenol	85%	[127]
CuMn$_2$O$_4$	RhB and MO	97% and 57%	[128]
NiS−P zeolite	EBT	~62%	[42]
CdS-ZnS	Rifampin	~84%	[43]
Ag halides-clinoptilolite	4-MA and 4,3-CNA	~40% and ~41%	[129]
B-TiO$_2$	Metoprolol	70%	[130]
Ag nanoparticles and TiO$_2$	Formaldehyde	~95%	[131]
Fe-TiO$_2$	Phenol	~60%	[119]

Excitation of an e$^-$ from its VB to CB occurs when photons get absorbed by photocatalyst, leaving behind a positively charged h$^+$. The redox processes occur at the catalyst surface and the consequence is the reduction of contaminants. If these e$^-$-h$^+$ pairs are not immediately scavenged after photo-excitation, they are combined and neutralized rapidly, a phenomenon known as recombination. This can happen on the nanomaterial surface, known as surface recombination, or in bulk, known as mass recombination. Recombination cause energy to be released, leading to reduction of quantum efficiency. This process can occur on the surface or within the bulk of the catalyst due to various problems in crystal defect sites. The introduction of dopants, co-catalysts, or heterogeneous coupling can be used to avoid or minimize recombination reaction [27,92,123,129,132]. Thus, heterogeneous photocatalyst becomes VLA with significant changes in the crystal structure. Reducing technique of recombination of semiconductor is further discussed in section 5.

4. Photocatalytic Disinfection by Using VLA TiO$_2$ Nanohybrids

4.1 Photodegradation of Microorganisms

Since the fundamental mechanism of inactivating microorganisms through nanotechnology is yet to be thoroughly explored, there is no precise method to

justify the disinfection phase. Two hypotheses can be used to describe the disinfection mechanism regarding microbes. There are (1) free metal ions released from metal-semiconductor materials by dissolution and (2) oxidation of cells by utilizing ROS generated on the semiconductor surface. Furthermore, since the outer charge of microbe cells is negative, the positive charge on the semiconductor increases their adsorption onto a nanoparticle. As a result, it will have an immediate impact on the disinfection process [109]. **Table 2** shows a toxic level of free metal ion concentration for various microbes. Metal ions show toxicity against microbes in several ways including deactivation of enzymes [133], denaturing protein, destroying nucleic acids, hindering cell multiplication [134], growth inhibition, inhibition of O$_2$ transferability[135] and death [136].

Table 2. Toxicity of Heavy Metals against Microorganisms

Microbe	Species	Metal	Toxic level/ppm	Tolerable level/ppm	Reference
Bacteria	*Bacillus subtilis*	Cr	>100	<50	[137]
	E.coli		9-10	<60	
	Staphylococcus spp.	Pb	>1	<0.8	[138]
	Streptomyces spp.		>1	<0.8	
	Staphylococcus spp.	Cu	>1.5	<1.0	[138]
	Streptomyces spp.		>1.5	<1.0	
	Pseudomonas spp.	Ni	>1.0	<0.5	[139]
	Acinetobacter spp.		>50	<35	[140]
	Enterobacter cloacae	Co	>10	<8	[141]
	Pseudomonas aeruginosa	Hg	>50	<35	[141]
	Klebsiella pneumoniae		>50	<35	[142]
	Pseudomonas spp.	Zn	>0.5	<0.5	[139]
Fungi	*Sphaerotilus natans*	Cr	>100	<80	[143]
	Phanerochaete chrysosporium		>10	<10	[144]
	Candida albicans	Hg	>0.03	<0.02	[145]
	Candida maltosa		>0.04	<0.03	
	Candida albicans	Ag	>0.02	<0.01	[145]
	Candida maltosa		>0.04	<0.03	
	Aspergillus flavus	Pb	>1000	<1000	[146]
		Zn	>1000	<1000	
		Ni	>1000	<1000	
		Cu	>100	<100	
		Cd	>100	<100	
		Cr	>100	<100	
	Aspergillus niger	Cr	>100	<100	[146]
		Pb	>1000	<1000	

		Cu	>500	<500	
		Zn	>250	<250	
		Cd	>100	<100	
		Ni	>100	<100	
Algae	*Spirogyra* spp.	Cr	>5	<5	[147]
	Spirulina spp.		>5	<5	
	Chlorella vulgaris	Pb	>5	<3	[148]
		Cu	>1.5	<1	[149]

The photocatalyst has been demonstrated to destroy a wide range of microbial species, including Gram-negative and Gram-positive organisms, fungi, algae, protozoa, and viruses. It has also been demonstrated to be capable of inactivating toxins by microorganisms using semiconductors [109,150,151]. The ability to destroy microbes indicates that the surface of nanohybrids can be self-sterilizing, particularly when modified with transition or noble metals [109].

Gram-negative bacteria (GN)

E. coli is a representative of GN bacteria, has a thin peptidoglycan layer (much thinner than in GP) and an outer membrane with lipopolysaccharide (LPS) in the outer layer and phospholipids in the inner layer. The high lipid content of GN in the outer membrane makes it special than GP [152].

Gram-positive bacteria (GP)

As a representative of GP, *Staphylococcus aureus*, has a thick peptidoglycan coating that covers more than half of its surface area, generally about 90% of the total area. The peptidoglycan consists of a crystal lattice structure in the bacterial cell wall, produced by two amino sugars, namely, N-acetylglucosamine and N-acetylmuramic acid, respectively [109,152].

The significant resilience of GN cell wall to dissociation is well established. The presence of high levels of LPS and proteins in the outer membrane, along with a limited number of phospholipids, are the crucial molecules in the membrane's superior chemical resistance activity. Due to the outer membrane barrier, GN bacteria is more resistant to dissociation than GP, however the mechanism of resistance is still unknown to the scientific world. Although photocatalysis' antibacterial activity has not been fully investigated, the sterilizing process mechanism is still unclear [152].

Fungi, algae, and protozoa

Under the laboratory conditions, fungi spores are more stable than vegetative ones, and *Trichoderma harzianum* spores were resistant to destruction [153]. During the entire treatment period, *Acanthamoeba* cysts proved to become half of the cell reduction process [154].

Viruses

The majority of the tests were carried out using deactivated *E. coli* bacteriophages, which are demonstrated for ssRNA viruses (MS2 & Qβ), ssRNA virus, ssDNA type virus, and dsDNA type virus (λ & T4 Mammalian infections include (poliovirus 1), birds and human influenza viruses, and SARS coronavirus. The Zika virus is spread by mosquito vectors, as is the herpes simplex virus [109]. The mechanism of virus cell structure disintegration using photocatalytic technique is shown in **Fig. 7**.

Bacterial toxins (Cyanotoxins)

Photodegradation detoxified bacterial toxins are formed by GN bacteria endotoxin, algae toxins, and cyanobacteria toxins [109]. The adsorption and photocatalytic degradation of Microcystin-LR is greatly enhanced when a VLA N–TiO_2 nanomaterial is used under acidic conditions. It was proposed that electrostatic attraction between MC-LR and N–TiO_2 improved while MC-LR had a negative charge due to the disintegration of its free –COOH pairs, while N–TiO_2 had a positive charge [156,157].

More works related to bacteria/fungi/virus photocatalytic deactivations are present in **Table 3**. VLA photocatalysts obtained ~100% removal efficiency, suggesting VLA photocatalyst is a promising material to utilize in disinfection applications.
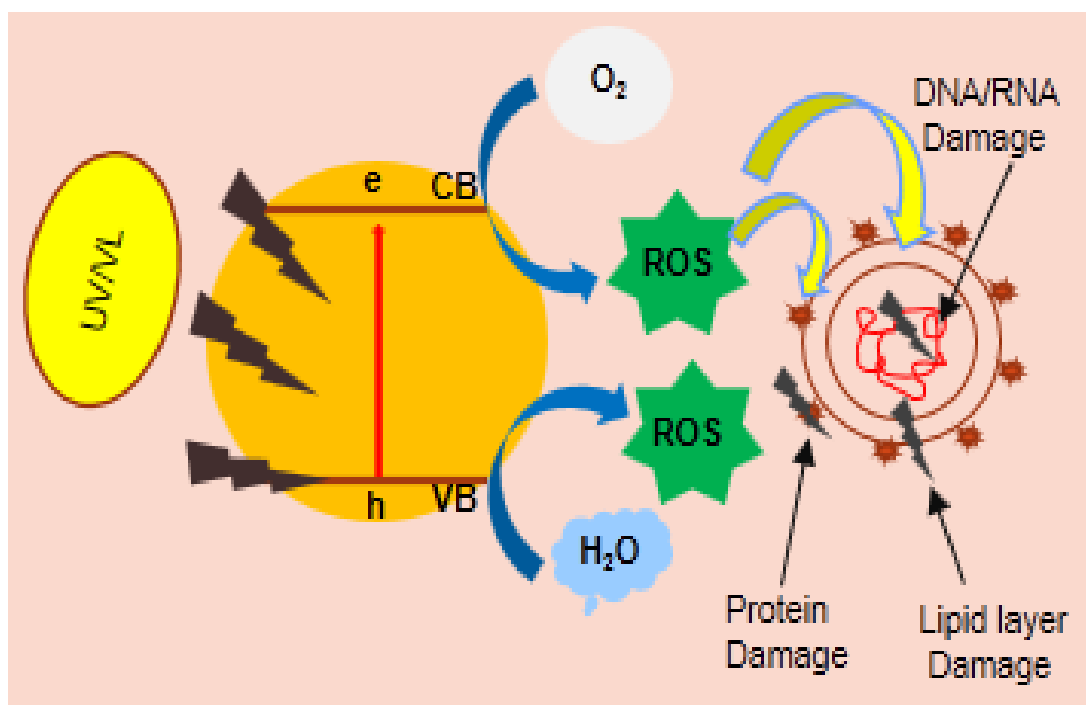
Fig. 7. Photocatalytic Deactivation Mechanism of Virus Cell using Semiconductor [155].

Table 3. Photocatalytic Activity against Various Microbes

Microbe	Species	Photocatalyst	Efficiency (%)	Reference
	E. coli	N-TiO$_2$	100	[158]
	Staphylococcus aureus	Ce/B-TiO$_2$	100	[159]
	E. coli	V/N-TiO$_2$	100	[160]
	E. coli	BiOBr-AgBr	100	[161]
	E. coli	BiVO$_4$/Ag$^+$	>99	[162]
	E. coli	AgI/Bi$_2$MoO$_6$	100	[163]
Bacteria	*Staphylococcus aureus*	AgI/Bi$_2$MoO$_6$	100	
	E. coli	Porous g-C$_3$N$_4$ nanosheets	100	[164]
	E. coli	Ag/g-C$_3$N$_4$ nanosheets	100	[165]
	Staphylococcus aureus	Ag/g-C$_3$N$_4$ nanosheets	100	
	E. coli	Ag$_2$WO$_4$/g-C$_3$N$_4$ heterojunction	100	[166]
Fungi	*Candida* spp.	TiO$_2$	65	[167]
	Aspergillus niger	Cu/P-25	100	[168]
Virus	bacteriophage Qβ	Cu$_x$O/TiO$_2$	99.99	[169]

4.2 Disinfection Using Reactive Oxygen Species (ROS)

As a result of TiO_2 structures to create ROS, several studies have concluded that $^{\cdot}OH$ is a cell invader [170,171]. It is also possible to disinfect using ROS species such as superoxide ($O^{\cdot}_2$), H_2O_2, and O_3. However, $^{\cdot}OH$ redox potential (2.80 eV) is more suitable for microbial cell structure breakdown. Thus, $^{\cdot}OH$ become promising radical species to deactivate microbes [101]. Lipid peroxidation by ROS is shown by the release of chemical malondialdehyde (MDA) as a byproduct and a simultaneous loss of respiratory layer action as determined by a decrease in 2,3,5-triphenyltetrazolium chloride [171]. The $^{\cdot}OH$ generated by TiO_2 attack on dimethylsulphoxide and cysteamine is thus eliminated from the water [172]. Kikuchi *et al*. [173] demonstrated that *E. coli* slaughtering continued even though the bacteria were isolated from the surface by a 50 m thick porous layer. In any case, mannitol, a free radical scavenger, discouraged destroying without the membrane, although H_2O_2 catalase reduced destroying both with and without the microbes membrane. The hypothesis suggested that $^{\cdot}OH$ and peroxide were responsible for destroying close to the TiO_2 surface, with H_2O_2 acting as a stand-in at a certain distance. ROS, like peroxide radicals ($O_2{^{\cdot}}^-$), were not taken into account. The $^{\cdot}OH$ radicals generated by microwave irradiation of TiO_2 tended to improve the destruction of Gram-negative *E. coli* bacteria. Cho and Yoon [174] demonstrate that dominant ROS species destroy *C. parvum* cysts.

4.3 Mechanism of Disinfection

TiO_2 based nanohybrids offer a significant benefit due to their non-contact antibacterial activity. Furthermore, TiO_2 offers no toxic material release, avoiding harmful effect for human health and the environment, TiO_2-based structures are suitable for immobilization onto a substrate and/or insertion in vectors. Therefore, TiO_2 has become common semiconductor material that is used widely for disinfection applications. The antimicrobial activity was initially suggested to reduce coenzyme-A dimerization and, as a result, inhibit biological oxygen utilization. In either case, proof exists that the harmful behavior is caused by a cell membrane and cell wall damage. These effects are described based on (1) microscopy (2) lipid peroxidation discovery (3) leakage of intercellular elements such as ions, RNA, and protein and (4) spectroscopic analysis [109].

Loss of permeability leading to cell spillage of cellular components revealed the immediate spillage of K^+ ions from cured cells of *Streptococcus sobrinus;* AHT is generated within a short time. This is accompanied by a gradual release of RNA and protein. Spillage of K^+ also tended to be associated with cell death in GN bacteria such as *E. coli* [175,176]. Using TEM images of photocatalyzed cells of *S. sobrinus* with TiO_2, it was discovered that the cell division was disturbed and disintegrated after cells encountered TiO_2 photocatalytic activity for one hour of light irradiation, with more disruption after 2 hours [177]. Cell passing, according to scientists, is accompanied by changes in cell permeability and a strengthening of the cell wall structure. SEM images of different GN and GP revealed morphological changes that cause cell wall destruction after UV-A light on apatite-coated TiO_2 textures on cotton [178].

In the use of a thin layer of TiO_2 particles to destroy *E. coli*. the exterior film in the bacteria seemed to be affected. Following that, the cytoplasmic layer is degraded completely. Photocatalytic destruction happened, but there was no peptidoglycan degradation reaction. An instrument such as Atomic Force Microscopy (AFM) would estimate cells on irradiated TiO_2 film that appeared to have disintegrated external membranes [178].

Lipid peroxidation using ROS- Lipid peroxidation *via* ROS was illustrated by the discharge of MDA as a byproduct and simultaneous loss of respiratory film movement measured by the decrease of 2,3,5-triphenyltetrazolium chloride [172]. The degradation reaction of *E. coli* endotoxin occurs without substantial degradation of peptidoglycan; authors demonstrated that in GN bacteria, cell damage occurs in the following order: OM, PG, IM [179].

This study suggested that DNA damage could enable TiO_2 nanoparticles to move through cell membranes. Damage to DNA does occur on TiO_2, but it is most likely a recent occurrence following membrane dissociation and, eventually, cell death [180].

In spectroscopic studies, TiO_2 movement on disconnected two layer phospholipid has been observed, resulting in disruption of the two-layer structure using X-ray diffraction, laser spectroscopy, and Fourier Transform infrared spectroscopy (FTIR). The disruption occurred as a result of lipid peroxidation [181,182] as calculated by MDA growth. As reactive oxygen species (ROS) attack polyunsaturated fatty acids, such as linoleic corrosive, lipid peroxidation occurs. According to the FTIR spectra, *E. coli* allowed the development of carboxylic acids such as MDA as byproducts of membrane degradation. MDA also promotes decomposition by more extended irradiation periods [175]. **Fig. 8** depicts the commonly proposed
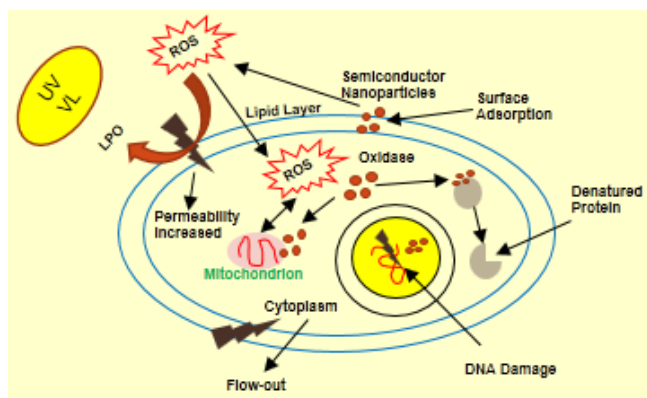
Fig. 8. The Proposed Mechanisms of Bacterial Cell Damage by using Semiconductor [183].

mechanism of cell disintegration reaction processes using semiconductor materials.

5. Synthesis of Synthetic TiO₂ and Natural Based TiO₂ Nanohybrids

5.1 Synthesis of Synthetic TiO₂ Nanohybrids

TiO₂ nanohybrids were synthesized by utilizing commercial Ti metal precursors. Due to its high Ti content, preparation of nanomaterials become very easy and quick. Titanium dioxide nanohybrids can be synthesized from several methods like sol-gel method [184–186], solid-state reactions, hydrothermal treatment [48,120], ultrasound-induced method, supercritical drying [187,188], coprecipitation [189], chemical vapor deposition [189,190], continuous reaction method, multi-gelation technique, Radio Frequency (RF) sputtering, microemulsion [191,192], Aerogel and Xerogel [190], plasma [189,191], wet impregnation [97,189], microwave-assisted method [25,52]. Some of the methods have been explained below.

The sol-gel method is a far more comfortable and conventional technique for the synthesis of TiO₂ nanoparticles. Thus, more authors prefer to follow the sol-gel route with changing different parameters (like the concentration of precursor, pH, solvent, *etc*.) to achieve TiO₂ particles [193]. The sol-gel method has advantages such as particle size, being controlled, leading to a higher surface area to particles [194]. The sol-gel process initiates from alkoxide, sulfur, and chloride-based precursor hydrolyzed into a "sol" and followed by polycondensation to create a "gel." Afterward, drying the gel converts to xerogel by evaporation of solvent and ultimately calcined amorphous powder changes into stable TiO₂ particles [193,194]. Guillard C. *et al*. showed excellent resistance to titanium alkoxide's hydrolysis rate *via* an esterification reaction. An acidic acid is applied to

regulate the hydrolysis, stabilize sol, and to avoid the precipitation of TiO₂ [195].

Hydrothermal method is ordinarily carried out in a steel vessel called autoclave consists of Teflon (poly-tetrafluoroethylene) liners beneath which regulate temperatures and weights watery arrangement. This strategy offers high purity nanosized TiO₂ at a moderate temperature with the least contamination. This method helps to reduce the production cost of nanosized TiO₂ materials [196].

Chemical vapor statement (CVD) – the method is based on the reaction between vaporizable metal alkoxides (e.g., isopropoxide) and oxygen or steam of gases. These forms are ordinarily utilized to create coatings to manipulate the various properties of different substrates. It happens inside a vacuum chamber, and the thermal energy supply heats up inside gases within the coating chamber as a result, a thin layer of material is deposited on the substrate [196].

The sputtering was developed very useful to synthesize nanosized TiO₂ particles. This strategy employs plasma made from argon and oxygen atoms. Energized argon (Ar) ions hit an anode made from TiO₂ or evaporated Ti, deposited on a substrate [196].

Microemulsion method is characterized as the thermodynamically stable, optically isotropic fluid of two or three immiscible liquids with the addition of surfactant. It gives a heterogeneous mixture for nanoparticle synthesis. The arrangement of particles in frameworks is governed by the reactant dispersed within the droplets. The steady surfactant microcavities give a hindrance impact that limits nucleation reaction, reducing particles' development and aggregation. It happens in two ways: direct microemulsion (oil in water) and reservoir microemulsion (water in oil), equivalent to fluid and non-liquid media. The micelles are shaped in a liquid medium, where hydrocarbon chains of surfactants are situated toward the micelle's insides. The hydrophilic head of the surfactants is attached with the encompassing watery medium [48].

A few types of Ti metal precursors are used to synthesize nanohybrids, namely, alkoxide [186,197,198], chloride precursors [187,199,200], sulfur precursors [188,201], *etc*. The commercially available TiO₂ material is the Degussa P-25 [202,203], and anatase [13,202]. In the sol-gel method, various other chemicals are also used such as solvents [24,199], stabilizers [86] and surfactants [99,204,205] that can be identified from the literatures. **Table 4** shows the advantages and disadvantages of TiO₂ synthesis methods.

Table 4. The Advantages and Disadvantages of Various TiO_2 Synthesis Methods

Method	Advantages	Disadvantages	Reference
Sol-gel	Easy, Homogeneity, Reproducible	High cost, required high temperature to calcine	[206]
Chemical Vapor Deposition	Uniform, pure and reproducible particles	Slow evaporation of solvent, aggregation occur	[207]
Hydrothermal	Simple, high-quality crystals	Required expensive autoclave unit	[208]
Sputtering	High quality and uniform particles	Ionic bombardment	[209]
Microemulsion	Particle size can be controlled	High cost for emulsion	[210]

5.1.1 Metal or Metals Doped TiO_2

More metals were used as a dopant to attach with TiO_2, and attempts were successful enough to enhance photocatalytic activity. Numerous metals have been used to modify the titania structure and its BG values. Among the metals, transition metals (like Fe, Co, Ni, *etc*.) [51,79,120], noble metals (like Ag, Au, Pt, and Pd) [20,112,211,212], lanthanide metals (like La, Nd, Pr, *etc*.) [213] are used by different researchers to produce promising photocatalyst.

The first attempt of non-metal doping was in 1986, when nitrogen (N) is used as the doping element with TiO_2. After that, more different non-metals have been used as a dopant by various authors. Moreover, a non-metal doped photocatalyst has been modified to absorb VL while narrowing the BG. Thus, it enhance the photoactivity under visible range as well [191]. More different non-metals (N, B, C, S, *etc*.) [56,108,118,191] were used by authors for doping to TiO_2 crystal structure.

5.1.2 Nanocomposite of TiO_2

The nanocomposite comprises of two or more metal oxides mixed and forms somewhat different material (Example: SiO_2/TiO_2) which enhances the absorption of VL, thus influences greater photoactivity. Nanocomposite is synthesized by using Graphene oxide (GO), ZnO, V_2O_2, SnO_2 [13,80,197,214]. Authors interpret nanocomposite a very promising photocatalyst to be used to decompose organic pollutants.

5.2 Synthesis of Natural Based TiO_2

A few scientists evaluated the structure of the Earth's crust to be 16 % alumina, 7% iron oxides, 4% magnesium oxide, and 1% titanium dioxide, which makes titanium the fourth primary abundant support metal in the world. Titanium (Ti) is the ninth most abundant element [215]. The various minerals containing Ti metals and their physical properties are shown in the **Table 5** [216]. Ti overwhelming mineral forms are Ilmenite (ferrous iron $FeTiO_3$) and rutile (TiO_2). Other minerals contain an exceptionally minor amount of Ti. The primary use of Ilmenite is the generation of TiO_2 white pigment *via* the sulfate and chloride routes [217]. Rutile is utilized in welding rod coatings and making titanium metal. Recently rutile is utilized for the generation of TiO_2 white pigments *via* the chloride route. Pure Ilmenite contains 32% Ti and 37% Fe [215,217]. As compared, rutile has 60.0% Ti and 40.0% O and much better titanium mineral for the generation of pigments [217], the sulfate route generates approximately 3.5 tons of waste. In contrast, the chloride route generates only 0.2 tons of waste per ton of TiO_2. In the sulfate route, iron sulfate ($FeSO_4$) formation is considerably more significant than $FeCl_3$ from the chloride route. Moreover, the production cost and extreme acid treatment are required for extraction of Fe in the sulfate route [218]. The quality of TiO_2 pigment depends on Fe removal efficiency. Higher the Fe removal ability will increase the purity of TiO_2. Therefore, the synthesis route very much depends on the chemical used in the process. Iron removal efficiency decreased in following order, $HF>H_2SO_4>HCl>HNO_3$ [219]. The significant quantity of Ilmenite is provided by United States, Australia, Canada, European countries, Asian countries, and African countries, and the significant rutile producers are Australia, African countries, and India [216,217]. Nowadays, more than 50% of the world's rutile is used to pigment manufacturing industry. Less than 15% of Ti's entire world supply now comes from rutile, and the ores of rutile decreased to approximately 30% of the Earth's Ti ores due to the demand in mining process [216].

Table 5. Major Ti Containing Minerals Present in the Earth Crust and Their Physical Properties

Mineral	Specific gravity	Hardness (Mohs)	Color
Ilmenite ($FeTiO_3$)	4.74	5.50	Black
Rutile (TiO_2)	4.37	6.25	Reddish brown
Anatase (TiO_2)	3.90	5.75	Brown
Brookite (TiO_2)	4.13	5.75	Yellowish brown
Leucoxene (TiO_2)	4.00	-	Yellowish brown
Arizonite ($Fe_2O_3.3TiO_2$)	4.12	-	Deep red

5.2.1 Sulfate Route

The sulfate route, powdered Ilmenite, or slag (acid-treated Ilmenite) (78% TiO_2) interacted with sulfuric acid, then the final product as titanium sulfate ($TiSO_4$) increased to make a TiO_2 pigments and waste comprising majority of ferrous sulfate heptahydrate ($FeSO_4.7H_2O$) crystals. The commercial extraction of TiO_2 from sulfate route started in 1918 in the US and Norway. The $Fe_2(SO_4)_3$ solution was reduced with iron to $FeSO_4$, after which the mixture cooled down to crystallize the iron into $FeSO_4.7H_2O$. The supernatants react with acid and TiO_2 to accelerate the TiO_2 formation as fine colloidal particles. The washing process of solids removes the iron and other impurities (anions like SO_4^{2-}, Cl^-, cations like Mn, Si, Mg, *etc*.). TiO_2 pulp is calcined in a rotary kiln machine to evacuate water and generate the perfect TiO_2 crystals. Only Ilmenite is used in this route because rutile and leucoxene are not reacting with sulfuric acid [216,220–222].

5.2.2 Chloride Route

rutile, synthetic rutile, or high-Ti slag (or Ilmenite 61% TiO_2) can reacts with chlorine gas (Cl_2) to generate titanium tetrachloride ($TiCl_4$). The titanium tetrachloride was purified to achieve less impurity level. This was followed by conversion directly to TiO_2 pigment with the discharging Cl_2 by warming the vapor with air at elevated temperatures. In contrast to the sulfate route, this process produces less waste (e.g., $FeCl_2$ can convert to FeO very quickly). The chloride process undergoes two steps. (1) The primary step is the rutile reacted using coke (C) as a reductant and Cl_2 as the reacting gas to make $TiCl_4$ and a small residue (waste), (2) $TiCl_4$ is burned with O_2 at elevated temperatures in an especially design burner to generate TiO_2 pigments [215,216,223].

5.2.3 Microbiological Oxidation

The microbiological oxidation route is also used rarely to separate Ti metals from Ilmenite minerals. The bioleaching is less productive than acid leaching in terms of Ti and Fe extraction. The bioleaching experiments after 35 days brought about very low Fe and Ti dissolutions with utilizing pure cultures (*A. niger*, *P. citrinum*, and *B. megaterium*) and mixed cultures (*A. niger* and *P. citrinum*) [224].

5.2.4 Alkaline Route

Amer [225] reported the primary roasting method from dissolving Ti from mechanically stimulated Ilmenite. About 90% of Ti was leached by generating sodium titanate (Na_2TiO_3) under the ideal conditions. Alkaline roasting is commonly utilized to disintegrate Ti from Ilmenite or the acid-treated titania solids after leaching out of iron. The blend of NH_3 water and H_2O_2 was used for dissolving Ti from acid-treated titania solids [226, 227]. **Table 6** shows natural-based visible, active TiO_2 nanohybrids synthesized methods and utilized as photo catalytically applications.

5.3 Characterization of Synthesized VLA TiO_2 Nanohybrids

Since the preparation of TiO_2 needs to identify what material is present in the synthesized sample, nanomaterials cannot be observed from the naked eye. Therefore, by using high tech instruments such as X-ray Diffractometer (XRD), Scanning Electron Microscope (SEM) coupled with Energy Dispersive X-ray spectroscopy (EDS), Transmission Electron Microscope (TEM), X-ray Photoelectron Spectroscopy (XPS), Fourier-Transform Infrared Spectroscopy (FTIR), Raman Spectroscopy (Raman), Brunner–Emmett–Teller (BET) and Barret, Joyner, and Halenda (BJH) pore size distribution, UV-Visible Diffuse Reflectance Spectroscopy (UV-Vis-DRS), Thermogravimetric Analysis (TGA/DTA) and Electron

Table 6. Natural Based TiO_2 Nanohybrids Synthesized from Ti Contained Natural Minerals

Raw material	Method	Nanohybrid	Application	Reference
Rutile	-	-	MB oxidation	[228]
Ilmenite	Sulfate	Synthetic anatase	MO oxidation	[229]
Ilmenite	Sulfate	Synthetic rutile	Cigarette smoke degradation	[230]
Ilmenite	Alkaline	$Li_4Ti_5O_{12}$	Electrochemical	[231]
Ilmenite	Alkaline & Chloride	Synthetic rutile	Oxalic acid	[232]
Ilmenite	Chloride	$LiFePO_4$	Electrochemical	[227]

paramagnetic resonance spectroscopy (EPR) were used to identify nanomaterials based om literature.

Moreover, researchers are willing to make sure that their anticipated material is present in the synthesized titania sample. As an example, solely phase is no more photoactive, thus need to have mixture phases. If the synthesized material purely present in one phase, no more photocatalytic activity occurred. Thus, it is a failure and those materials are not used. Therefore, characterization techniques are an important cause of supporting to identify what compounds are present in the samples. If dopant introduces to titania, the characterization method can confirm the dopant attached to titania by studying spectra given by the instruments. That is the critical factor concern with doping ions to the titania phase.

5.3.1 X-ray Diffractometer (XRD)

XRD may be a routine technique that decides a sample's composition or crystalline structure. Besides, crystals like macromolecules and inorganic compounds can be utilized to determine atoms' structure inside the sample. This method transmits X-ray beams from the x-ray tube. X-rays are chosen since the wavelength is analogous to dispersing between particles within the sample, so diffraction is disturbed by spreading the molecules within a particle. The x-rays pass through the sample, leaping off the particles within a structure, and changing the beam's direction at a different angle, theta θ, from the original beam. Usually, the point of diffraction. The point of diffraction can at that point utilized to decide the contrast between nuclear planes operating Bragg's law (Equation 16) [25].

$$d = \frac{k\lambda}{\beta \cos\theta} \qquad (16)$$

Where, d is the crystallite size, λ is the wavelength of the X-ray radiation (Cu Kα=0.15406 nm), k is the shape factor (0.9), β is the full width at half maximum of the most intense peak and θ is the diffraction angle. The distance between atomic planes can be used to determine the composition or crystalline structure [24,81,233].

The anatase and rutile phase mass fraction can be calculate *via* Spurr's equation (eq. 17) [98,187].

$$f_a = \left(1 + 1.26\frac{I_a}{I_r}\right)^{-1} \qquad (17)$$

$$f_r = (1 - f_a) \qquad (18)$$

$$\frac{A}{R} = \left\{\frac{f_a}{f_r}\right\} \qquad (19)$$

Where f_a & f_r are the anatase and rutile fractions and I_a, I_r are the integrated intensities of the most intense peaks of anatase (1 0 1) and rutile (1 1 0) (eq. 18), eq. 19 shows the fraction ratio of the anatase and rutile, respectively. The most intense peaks of anatase phase are 25.17°, 37.60°, 47.76°, 54.01°, 62.60°, 68.59°, 70.36° and 75.09° and its hkl values are 101, 004, 200, 105, 204, 116, 220,215, respectively (database card no. JCPDS-00-021-1276) [81,111,190], whereas rutile is 27.38°, 36.10°, 41.24°, 54.28° and 62.67° and its hkl values are 110, 101, 111, 211 and 002, respectively (database card no. JCPDS-00-021-1276) [81]. Also, brookite is 25.34, 25.69 and 30.80° and its hkl values are 120, 111, 211 (database card no. JCPDS-00-029-1360) [76,89,234].

5.3.2 Fourier-Transform Infrared Spectroscopy (FTIR) & Raman Spectroscopy (Raman)

Fourier-Transform Infrared Spectroscopy (FTIR)

IR spectroscopy consolidates a few sorts of estimation strategies, like diffuse reflection strategy and attenuated total reflection strategy (ATR). The procedure's guideline is the change in dipole moment in an atom due to its movement after absorbing the Infrared radiation could be a characteristic feature of the atomic species and attributes for a typical spectrum. This strategy

advantage is also famous as relatively cheap, fast, and simple to utilize and requires a small amount of sample [235]. **Table 7** shows FTIR peak positions of doped titania and pure titania.

Table 7. FTIR Peak Positions of Doped and Pure TiO_2

Functional group	Vibration type	Material type	Band position (cm^{-1})	Ref.
O-H water	Stretching		3240	
O-H adsorbed water	Bending	TiO_2	1623	[199]
O-H water	Stretching		3100-3600	
O-H adsorbed water	Bending		1630	
Ti-O	Stretching	TiO_2	722	[80]
	Bending		590	
Ti-O-Ti	Stretching		525	
	Bending		471	
O-H water	Stretching		3400	
O-H adsorbed water	Bending		1640	
Ti-O anatase	Stretching	TiO_2	550	[236]
Ti-O rutile	Stretching		530-640	
Ti-O & Ti-O-Ti	Bridging stretching		400-700	
O-Ti-O	Stretching	Cu/Zn-TiO_2	492-505	
	Stretching	TiO_2	458	[237]
	Stretching	TiO_2	3426	
O-H water	Stretching	Cu/Zn-TiO_2	3419-3426	
O-H water	Stretching		3416	
O-H adsorbed water	Bending	TiO_2	1644	[25]
Ti-O	Bending		670-735	

Raman Spectroscopy (Raman)

In Raman spectrometer, frequently, a modest fraction of the scattered light features a different color. It has changed frequency because, during the diffusing process, its energy changed by association with atomic vibrations. This is known to be the Raman diffusing process.

The primary stage in producing a Raman spectrum is to irradiate the sample with a unicolor light source, like a laser. Most of the light that disperses outside unaltered in energy known as "Rayleigh scattered." Raman change happens since photons interchange part of their energy with atomic vibrations in the material. The frequency of vibration of particles determines the interchange in energy [238]. **Table 8** shows Raman band positions of TiO_2 phases.

5.3.3 Brunner–Emmett–Teller (BET)

The BET philosophy (Brunner-Emmett-Teller theory) is utilized to decide the surface area of solid or permeable materials. Various properties such as disintegration rates, catalytic development, moisture retention, and shelf life are routinely related to a material's surface area. Total pore size distribution was analyzed using a cylindrical pore prototype of the BJH (Barret, Joyner, and Halenda) method [235]. **Table 9** shows the BET surface areas and BJH pore size distribution of different photocatalysts.

5.3.4 UV-Vis Diffuse Reflectance Spectroscopy

The light occurrence at optically dispersion interfacing (samples like powders) with coarseness reduces the wavelength may somewhat reflect frequently, incompletely scatter, and be partly absorb to the substrate. The last portion may experience absorption inside particles, experience deflection at grain edges, recur at the sample surface, and interact with reflected parts. In DRS, UV range proportion of the light scattered from a boundlessly dense layer and the scattered light from a perfect non-absorbing testimonial sample was measured as a work of the wavelength λ. The light of powdered samples by incident radiation leads to diffuse light of the tests. The incident light somewhat retained, to some degree scattered. The scattered radiation, transmitting from the sample, is collected in an integration sphere and identified [235]. The BG calculation is done by taking diffuse reflectance values (R) of the solid sample, which is transforming to Kubelka-Munk function shown in equation 20 [33,35,39,41,108,128].

Table 8. Vibration Frequencies and Observed Raman Bands (cm^{-1}) for Anatase, Rutile, and Brookite

Anatase		Rutile		Brookite		Reference
Position (cm^{-1})	Assignment	Position (cm^{-1})	Assignment	Position (cm^{-1})	Assignment	
134	E_g	433	E_g	-	-	
382	B_{1g}	591	A_{1g}	-	-	
503	A_{1g}	-	-	-	-	[54]
621	E_g	-	-	-	-	
155	E_g	466	E_g	-	-	
399	B_{1g}	610	A_{1g}	-	-	
513	$A_{1g} + B_{1g}$	-	-	-	-	[52]
634	E_g	-	-	-	-	
146	E_g	448	E_g	248	A_g	
397	B_{1g}	-	-	321	B_{1g}	[118]
516	A_{1g}	-	-	-	-	
638	E_g	-	-	-	-	
145	E_g	154	B_{1g}	126, 154, 196, 247, 413, 635	A_g	
197	E_g	239	combination	213, 323	B_{1g}	[239]
397	B_{1g}	446	E_g	366, 462, 585	B_{2g}	
639	E_g	609	A_{1g}	454	B_{3g}	
-	-	-	-	155, 194, 247, 412, 636	A_g	
-	-	-	-	213, 322, 501	B_{1g}	[89]
-	-	-	-	366, 395, 460, 583	B_{2g}	
-	-	-	-	172, 287, 545	B_{3g}	

Table 9. BET Surface areas and BJH Pore Size Distribution of Semiconductors

Material	Method	BET surface area/ m^{2}g	BJH Pore diameter/ nm	Reference
SnO$_2$-TiO$_2$	Chemical bath deposition	57.00	-	[80]
		33.00	-	
		103.00	-	
TiO$_2$	Sol-gel	53.73	-	[190]
TiO$_2$	Sol-gel	25.50	8.80	[54]
	Solution combustion	177.00	3.85	

	Microwave assisted hydrothermal	250.00	8.80	
Mesoporous TiO$_2$	Sol-gel	78.51	44.32	[240]
		110.73	16.80	
TiO$_2$	Hydrothermal	163.00	6.70	[81]
	Commercial	31.00	-	
TiO$_2$	Co-precipitation	202.00	3.90	[241]
Fe/Co/Ni-TiO$_2$		182.00-199.00	3.90-4.30	
TiO$_2$	Sol-gel	104.00	-	[120]
Cu/Fe/La-TiO$_2$		110.00-130.00	-	
P-25	Commercial	50.00-54.00	-	[56]
Rutile	Sol-gel	303.40	6.50	[234]

$$F(R) = \alpha\left[\frac{(1-R)^2}{2R}\right] \qquad (20)$$

$$\alpha\left\{(h\upsilon)^{\frac{1}{m}}\right\} = C\left(h\upsilon - E_{bg}\right) \qquad (21)$$

By using equation 21 and optical BG value as *m*=2 for direct transition for Tauc plot of $(F(R)h\upsilon)^2$ vs bang gap

energy (E_{bg}) will determine the BG value of the photocatalyst sample [39,83,108,129,242]. **Table 10** shows the calculated band gap values of various semiconductors materials prepared from different methods.

Table 10. The Band Gap Values Obtained for Various Semiconductors

Material	Band gap (eV)	Reference
TiO$_2$	3.09	
Ni/Mn-TiO$_2$	3.07	[186]
	3.08	
Pure Anatase	3.25	
Pure Rutile	3.00	[236]
Mixed phase	3.00-3.25	
Pure TiO$_2$	3.30	[237]
Cu/Zn-TiO$_2$	3.00-3.20	
Co-NiAl$_2$O$_4$	2.80-3.00	[33]
CuMn$_2$O$_4$	3.00	[128]
PbS-CdS	2.69	[41]
AgCl-AgI/NCP	2.82	[129]
CuO-ZnO/NCP	3.20	[39]
NiO-PbO-NCP	3.36-4.29	[35]

NCP-Natural Zeolite nanoparticles

5.3.5 X-ray Photoelectron Spectroscopy (XPS)

X-ray photoelectron spectroscopy for chemical examination may be a simple investigation strategy that gives primary and chemical state data from the external 5-10 nanometers of a solid surface. X-ray of known energy (hν), for the most part, Al (Kα) at 1486.7 eV or Mg (Kα) at 1253.6 eV, interatomic with a molecule, a photoelectron transmitted by incomes of the photoelectric effect. Chemical information in nearly the sample can be extricated since holding energies are dependent on the chemical environment of the molecule. Chemical environments that deshield the atom of interest causes that particle's center electrons to extend binding energies. Alternately, diminished binding energies are measured for the center electrons of molecules that pull back electrons from others.

X-rays (photons) assaulted a sample, and when electrons inside the sample retain adequate energy, they are evacuated from the sample with a particular active energy. The energy of eliminated electrons was analyzed by the detector and plot of these energies and relative numbers of electrons. Electrons of particular energies follow distinctive ways through the sensor, which allows the computer to recognize the electrons and create the spectra [235]. **Table 11** shows XPS binding energies of TiO_2 synthesized from various methods.

Table 11. The XPS Binding Energies of TiO_2

Material type	XPS peak	Binding energy (eV)	Reference
	Ti $2p_{1/2}$	458.5	
	Ti $2p_{3/2}$	464.2	
Anatase	Ti^{+4}	458.6, 464.4	[81]
	Ti^{+3}	457.3, 463.2	
	C 1p	199.2	
	Ti $2p_{1/2}$	464.3	
	Ti $2p_{3/2}$	458.5	
Anatase	O 1s (O^{2-})	529.8	[243]
	O 1s (OH)	531.0	
	C 1s	285.0	
S-TiO_2	N 1s	401.2	[118]
	O 1s	530.5	
	S 2p	169.7	
	Ti 2p	460.8	
	C 1s	284.6	
N-TiO_2	N 1s	399.0	[108]
	Ti $2p_{3/2}$	457.9	

Ti^{+3}	456.5
O 1s (O^{2-})	529.0
O 1s (OH)	529.7

5.3.6 Scanning Electron Microscope (SEM) coupled with Energy Dispersive X-ray spectroscopy (EDS) & Transmission Electron Microscope (TEM)

Scanning Electron Microscope (SEM) coupled with Energy Dispersive X-ray Spectroscopy (EDS)

Generally, the morphological examination is sufficient to characterize a catalyst material as TiO$_2$, and the EDX investigation serves to confirm this characterization and recognizes the composition atoms display in TiO$_2$. The SEM uses a centered beam of high-energy electrons to create multiple signals at the surface of solid specimens. In most applications, data is collected over a chosen region of the surface of the sample. EDS utilized the X-ray range transmitted by a significant test assaulted with a strong beam of electrons to induce a localized chemical examination. The qualitative investigation includes identifying the lines in the content and is reasonably direct due to X-ray spectra's easiness [235]. Anatase particles are spherical shaped, rutile particles are needle/spindle-shaped, whereas brookite has an ellipsoidal/cylindrical structure [54,185,234,244]. Anatase crystal size varies from 10-20 nm as indicated in the publication [54].

Transmission Electron Microscope (TEM)

The TEM may be a viable device for energetic material testing. An energized beam of electrons transfers through a sample. The contacts between the electrons and the particles are utilized to observe topographies such as the crystal configuration and grain edges. The electron beam from the electron gun was reduced into a small, consistent by a condenser lens. The beam strikes the sample, parts of the beams are diffused due to the sample's depths and electron opacity. This diffused beam is exchanged for a lens and a picture is made on the phosphor screen. The image passed down the narrow channel through the center of the lens; that point broadened all the way. The picture is shown up on the screen [235]. TEM images of anatase particles are spherical-shaped, rutile particles are needle shaped [52,54,244,245]. The crystallite size of the anatase is 5 nm and the needlelike rutile nanoparticles is 7 nm [234].

5.3.7 Electron Paramagnetic Resonance Spectroscopy (EPR)

Electron Paramagnetic Resonance (EPR) could be a portion of magnetic resonance spectroscopy, which utilizes microwave radiation to test elements with delocalized electrons, such as radicals within the remotely related inactive attractive field. EPR targets the interaction between an attractive external field and the unpaired electrons of any system, EPR is performed utilizing microwaves. In EPR, the frequency is regularly held steady, while the magnetic field quality is changed, EPR tests must frequently be performed at low temperatures [246]. Recent publications have recognized theelectron exchange from rutile to anatase electron catching sites by means of EPR [22,241]. The EPR values of anatase and rutile polymorphs are present in **Table 12**.

5.3.8 Thermogravimetric Analysis (TGA/DTA)

Thermogravimetric examination, TGA, is utilized to appear when a compound contains components such as solvents or other freely bound molecules that might disappear upon warming. Most heat flow into the sample holder (differential scanning calorimetry, DSC) can be measured and differentiated in temperatures between the test and reference pan (differential thermal analysis, DTA). DSC is quantitative, and it measures the total energy of the system [235]. The final weight loss (up to 900 °C) for pure, N-doped, and Ag-doped TiO$_2$ was just 3-4%. Water present on the catalyst surface evaporates at temperatures over 100 °C. Organic solvents and organic materials decompose at temperatures between 200 and 400 °C. No significant weight loss was detected above 400 °C, demonstrating the stability and purity of the catalysts produced [108]. Pure titania loses 32% of its weight across the whole temperature range examined, while doped titania loses 44%. TGA plot shows three phases to the overall weight reduction (percentage) due to the adsorbed water loss. From 150 °C to 400 °C, weight loss occurs due to chemisorbed water, solvent, and residual organics being removed. Over 400 °C, weight loss is minimal due to the stability of the catalyst [248].

Table 12. EPR Values for Anatase and Rutile

Phase	ERP Signals					Reference
	g_1	g_2	g_3	$g_\parallel$*	$g_\perp$#	
Anatase	2.016	2.012	2.002	1.958	1.988	[247]
Rutile	2.019	2.014	2.002	1.947	1.969	

*,# Surface Electron Trapping Sites; g_1, g_2 and g_3- surface hole trapping sites.

6. Recently Developed VLA TiO₂ Nanohybrid and Their Utility as Photocatalyst

This section contains recently synthesized VLA TiO₂ nanohybrid materials and their application as photocatalysts. Also, we introduce natural-based synthesized VLA TiO₂ nanohybrids and usage as environmental remediation.

Hydrogen and oxygen generation is one option to supply power by using a water oxidation reaction. Therefore, researchers try to generate VLA nanohybrids as a photocatalyst using VL as an energy source. The conventional water oxidation reaction occurred by using electrodes and electricity. Therefore, inventing a VLA photocatalyst reduces the cost of the water oxidation process and long-time reusable technique. Wang *et al*. [249] investigated a plasmonic photocatalyst based on

Au/TiO₂-rutile used as an O₂ generating nanohybrid for water-splitting reaction under VL irradiation. The nanocomposite Au/TiO₂-Ru/SrTiO₃: Rh photocatalyst is a promising material to produces H₂ and O₂ with the rate of 5.6 and 2.7 μmol/h/g, respectively. Miyoshi *et al*. [250] showed that nitrogen/fluorine-codoped rutile TiO₂ was synthesized using rutile TiO₂ and (NH₄)₂TiF₆. The TiO₂-N/F illustrated higher PCA; hence, H₂ and O₂ generation increased under VL irradiation. Hoang *et al*. [75] reported the N-Ta-TiO₂ nanowire catalyst showed a greater increment in photoelectrochemical reaction both under VL (>420 nm) illumination. Sinatra *et al*. [251] show the rate for H₂ production by using Au–Cu₂O (2 wt. %)–TiO₂ is slightly higher than Cu₂O (2 wt. %)–TiO₂, quicker than Au (2 wt. %)–TiO₂ and very much faster than TiO₂. **Fig. 9** shows the dye degradation with redox potential of VLA NaFeTiO₄ nanohybrid.
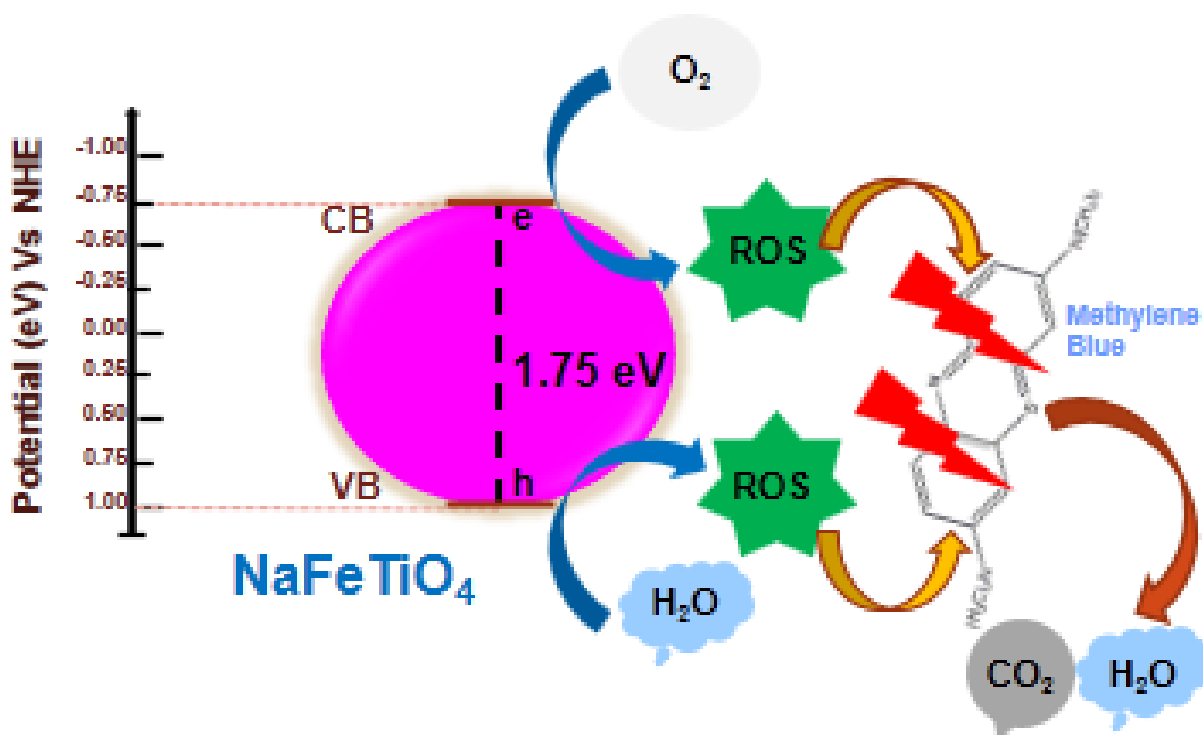
Fig. 9. Dye Degradation Under VL using VLA Heterogeneous Nanohybrid [252].

Hunge *et al.* [253] showed chemical oxygen values (COD) that mineralization of oxalic acid using WO_3/TiO_2 nanomaterial gave higher PCA and achieved 83% degradation. They suggested WO_3/TiO_2 VLA nanohybrid is a promising photocatalyst material regarding wastewater treatment. Zhu *et al.* [199] investigated VLA photocatalyst $BiVO_4/TiO_2/GO$ to decompose Reactive Blue-19 (RB-19) under VL irradiation. They showed the mentioned nanocomposite achieved the best degradation % of RB-19. Cavalcante *et al.* [130] showed from their results of metoprolol (MET), degradation significantly increased by doping with 5% B to TiO_2 (70 % of MET removed) compared to pristine TiO_2 (48% of MET removed). Niu *et al.* [254] successfully created B doping TiO_2 and material which was used to degrade Methylene Blue (MB) under VL illumination. They achieved more considerable degradation of MB by using a 6% B-TiO_2 hetero nanomaterial. More synthetic VLA TiO_2 nanohybrids have been designed just like N/B/Ag-TiO_2 [108], Se-TiO_2 [76], Fe/Co/Ni-TiO_2 [241], GO-TiO_2 [230], S-GO-TiO_2 [255], Carbon Quantum Dot (CQD)-TiO_2 [256], Ce-TiO_2 [257], $MoSe_2/TiO_2$ [258], In/Fe-TiO_2 [5], WO_3-TiO_2 [259], Ag/Fe/Sr-TiO_2 [260], Ta/N-codoped TiO_2 [75].

The natural Ilmenite-based TiO_2 nanohybrids are also promising material for the water and air purification process. Scientists have now developed Ilmenite based photocatalysts for treatment techniques instead of using synthetic photocatalysts [230,252,261–266]. The synthetic photocatalyst is more expensive than the Ilmenite based photocatalyst because of higher chemical cost and extreme conditions applied to the synthesized method. Therefore, Ilmenite based photocatalysts are low cost and easily synthesized *via* sulfate, chloride routes [262,263,265]. However, there is a little or no publications regarding VLA active Ilmenite based nanohybrids. Hence, we summarized UV and VL activated Ilmenite based photocatalysts and their utilization in air and wastewater treatment applications in this review.

The Ilmenite is capable of decomposing Reactive Black 5 (RB-5) under the acidic condition irradiated with UV light. Complete mineralization of RB-5 occurred using 2.0 g/L of catalyst concentration of Ilmenite within two-hour irradiation [267]. Chuan *et al.* [228] used natural rutile to degrade MB dye in wastewater. Natural rutile decomposed 50% of MB within three hours and 90% in 77 h and is finally mineralized within 119 h under UV light. Mahmoud *et al.* [262] synthesized Fe doped TiO_2 photocatalyst using the lixivium (filtrate) phase obtained by directly leaching Ilmenite with HCl acid. They successfully added Pt, Pd, and Ag metals to iron-

doped TiO_2. They invented photocatalyst synthesizing methods for the first time in history. They used these photocatalysts to degrade MB under UV and VL. Only Pd added Fe-TiO_2 showed better degradation under UV light. Under VL, Ag added Fe-TiO_2 photocatalyst showed higher degradation % than Pd, and Pt added Fe-TiO_2. Kostova *et al.* [229] synthesized the synthetic anatase by direct leaching with H_2SO_4 acid by using Ilmenite. The PCA of anatase prepared from Ilmenite concentrate was lower than that of the commercially Degussa P 25 nanomaterial. Rosli *et al.* [230] synthesized TiO_2/GO and used it to degrade cigarette smoke. The results showed integrated photocatalyst better than pure TiO_2, commercial P25, and TiO_2-rutile regarding cigarette smoke's removal efficiency. The graphite increases the light absorption ability of TiO_2 in the VL area. Therefore, the synthesized photocatalyst is very useful in purifying polluted air. Tao *et al.* [232] obtained nano TiO_2 rods from the wet treatment process using Ilmenite with NaOH and HCl. The nanorods showed excellent PC properties in the photodecomposition of oxalic acid. They also mentioned that synthesized material was more reliable than commercial rutile material. Smith *et al.* [263] also synthesized Fe doped TiO_2 from sulfuric acid leaching with Ilmenite. They used their photocatalyst to degrade 4-chlorophenol (4-CP) under VL. The results showed above 30% degradation of the 4-CP from sulfated Fe-TiO_2 nanohybrid under VL irradiation, which is much better than P-25 material. García-Muñoz *et al.* [268] modified Ilmenite *via* reduction under the H_2 atmosphereand prepared surface-modified Ilmenite photocatalyst. They used photocatalyst to degrade phenol in water. The results showed complete phenol decomposition at pH of 3 and 50 °C experiment conditions.

TiO_2/SBA-15 catalyst was synthesized by using Ilmenite as TiO_2 material and modified silica species SBA-15, creating a massive specific surface area of 386 m^2/g. It showed the highest PCA, and dimethoate degraded within seven hours under simulated solar light [261]. Lan *et al.* [264] synthesized carbon-nitrogen-sulfur doped TiO_2 using Ilmenite. The Ilmenite was acid leached by using sulfuric acid. After preparing C-N-S-TiO_2 nanomaterial, they used tetracycline as a pollutant to investigate PCA. The photocatalyst degrades >95% of tetracycline by using 30 mg L^{-1} within 150 min under VL illumination. Xia *et al.* [269] used raw Ilmenite to inhibit the growth of *E. coli* bacteria under VL irradiation. Ilmenite can produce O_2^- under VL irradiation. With superoxide radical addition of persulfate dramatically increased the rate of *E. coli* inactivation. Kalantari and Emtiazi [270] show the

antibacterial activity of Ilmenite and nano Ilmenite material. Their results showed nano-Ilmenite contained an antimicrobial effect under VL illumination and dark condition compared to raw Ilmenite.

7. Conclusions

We have profoundly described the current trends in the environmental remediation application of semiconductor-based photocatalysts. Most organic dye pollutants and other hydrocarbons can effectively be degraded within the VLA TiO_2 nanohybrids under VL irradiation. The photocatalytic field shows that semiconductor is a promising route to remediate the organic pollutants since it is very efficient utilization of sunlight as an energy source. The semiconductors may produce reactive oxygen species (ROS) when exposed to UV and VL. The ROS degrade pollutants comprehensively in the formation of environmentally friendly byproducts like CO_2 and water. Thus, no environmental pollution occurred by using semiconductors. Drawbacks of TiO_2 such as large BG

can be overcome by introducing various metals, oxides which leads to generate user-friendly photocatalyst while activating under VL as well. Hence, this paved the way to use a wide variety of applications developed regarding the photocatalytic field in recent years. Therefore, titania after modification of the BG enables to work under UV, and VL becomes the best semiconductor material among other semiconductors (ZnO, CdS, WO_3). Many TiO_2 synthesized routes available to follow up with low cost, easy techniques. The synthetic and natural pathway is predominately used to generate VLA photocatalyst. The synthesized physical characteristics of nanoparticles must prove the photocatalytic efficiency. The naturally available ilmenite and rutile are the raw material for future nanohybrids production. More investigations are still going on to synthesize the best photocatalyst for all environmental remediation. Thus, information included this review article provides a great platform to solve many problems regarding best photocatalyst exists in present day.

Abbreviations

UV: ultra violet	VL: visible light	CB: conduction band	VB: valence band	BG: band gap	NHE: Normal Hydrogen Electrode	PCA: photocatalytic activity	VLA: visible light active	PA: photoactive	e^--h^+- electron-hole pair
$\cdot OH$: hydroxyl radicals	AOP: advanced oxidation process	E_g: energy gap	ROS: reactive oxygen species	$h\upsilon$: photon	e^-_{cb}: electron at conduction band	h^+_{vb}: positively charged hole at valance e band	$O_2^{\cdot-}$: peroxide radical	CT: created catechol	HQ: hydroquinone
BQ: benzoquinone	BT: benzenetriol	HBQ: hydrobenzoquinone	PG: pyrogallol	GN: gram-negative bacteria	GP: gram-positive bacteria	IM: inner membrane	PG: peptidoglycan layer	OM: superficial membrane	MDA: malondialdehyde
RB 255: reactive blue 255	AR 206: acid red 206	DR 23: direct red 23	MG: malachite green	BPB: bromophenol blue	E102: tartrazine azo-dye	CR: congo red	4-MA: 4-methoxy aniline	4,3-CAN: 4-chloro-3-nitro aniline	EB: eriochrome black t

MB: methylene blue	AFM: atomic force microscope	FTIR: fourier transform infrared spectroscope	RF sputtering: radio frequency sputtering	CVD: chemical vapor statement	XRD: x-ray diffractometer	SEM: scanning electron microscopy	EDS: energy dispersive x-ray spectroscopy	TEM: transmission electron microscopy	XPS: x-ray photoelectron spectroscopy
Raman: Raman spectroscopy	BET: Brunner–Emmett–Teller BJH: Barret, Joyner and Halenda	UV-Vis-DRS: uv-visible diffuse reflectance spectroscopy	TGA/DTA: thermogravimetric analysis DSC: differential scanning calorimetry	EPR: electron paramagnetic resonance spectroscopy	COD: chemical oxygen values				

Acknowledgements

References

[1] V. Karunaratne, N. Kottegoda, A. De Alwis, J. Natl. Sci. Found. Sri Lanka 40 (2012) 3-8.

[2] Z.L. Wang, W. Wu, Angew. Chem. Int. Ed. 51 (2012) 11700–11721.

[3] N. Dasgupta, S. Ranjan, C. Ramalingam, Environ. Chem. Lett. 15 (2017) 591–605.

[4] T. Harper, IOP Publ. Ltd 14 (2003) 1-5.

[5] N. Castro-Alarcón, J.L. Herrera-Arizmendi, L.A. Marroquín-Carteño, I.P. Guzmán-Guzmán, A. Pérez-Centeno, M.Á. Santana-Aranda, Microbiol. Res. Int. 4 (2016) 55–62.

[6] M. Mandeh, M. Omidi, M. Rahaie, Biol. Trace Elem. Res. 150 (2012) 376–380.

[7] N. Kottegoda, C. Sandaruwan, P. Perera, N. Madusanka, V. Karunaratne, Nanosci. Nanotechnol.-Asia 4 (2015) 94–102.

[8] U.A. Rathnayake, T. Senapathi, C. Sandaruwan, S. Gunawardene, V. Karunaratne, N. Kottegoda, Chem. Cent. J. 12 (2018) 1-7.

[9] V.K. Wimalasiri, H.U. Weerathunga, N. Kottegoda, V. Karunaratne, J. Nanomater. 2017 (2017) 1–14.

[10] G.P. Gunaratne, N. Kottegoda, N. Madusanka, I. Munaweera, C. Sandaruwan, B.A.D. Madhushanka, U.A. Rathnayake, V. Karunaratne, Indian J. Agric. Sci. 86 (2016) 494–499.

[11] N. Kottegoda, C. Sandaruwan, G. Priyadarshana, A. Siriwardhana, U.A. Rathnayake, D.M. Berugoda Arachchige, A.R. Kumarasinghe, D. Dahanayake, V. Karunaratne, G.A.J. Amaratunga, ACS Nano 11 (2017) 1214–1221.

[12] N. Kottegoda, I. Munaweera, N. Madusanka, V. Karunaratne, Curr. Sci. 101 (2011) 73-78.

[13] R. Raliya, C. Avery, S. Chakrabarti, P. Biswas, Appl. Nanosci. 7 (2017) 253–259.

[14] R.S. Mulik, C. Bing, M. Ladouceur-Wodzak, I. Munaweera, R. Chopra, I.R. Corbin, Biomaterials 83 (2016) 257–268.

[15] I. Munaweera, J. Hong, A. D'Souza, K.J. Balkus, J. Porous Mater. 22 (2015) 1–10.

[16] A. Nezamzadeh-Ejhieh, S. Tavakoli-Ghinani, Comptes Rendus Chim. 17 (2014) 49–61.

[17] M. Nosuhi, A. Nezamzadeh-Ejhieh, Electrochimica Acta 223 (2017) 47–62.

[18] C. Madhusha, I. Munaweera, V. Karunaratne, N. Kottegoda, J. Agric. Food Chem. 68 (2020) 8962–8975.

[19] S. Fernando, N. Madusanka, N. Kottegoda, U.N. Ratnayake, in: Proceedings Int. Conf. Adv. Mater. Sci. Eng., Colombo, Sri Lanka, 2012, 1-7.

[20] D.B. Hamal, K.J. Klabunde, J. Colloid Interface Sci. 311 (2007) 514–522.

[21] Y. Zhang, J. Wan, Y. Ke, J. Hazard. Mater. 177 (2010) 750–754.

[22] G. Li, L. Chen, M.E. Graham, K.A. Gray, J. Mol. Catal. Chem. 275 (2007) 30–35.

[23] J.H. Carey, J. Lawrence, H.M. Tosine, Bull. Environ. Contam. Toxicol. 16 (1976) 697–701.

[24]A.M. Luís, M.C. Neves, M.H. Mendonça, O.C. Monteiro, Mater. Chem. Phys. 125 (2011) 20–25.

[25]M.B. Suwarnkar, R.S. Dhabbe, A.N. Kadam, K.M. Garadkar, Ceram. Int. 40 (2014) 5489–5496.

[26]J. You, Y. Guo, R. Guo, X. Liu, Chem. Eng. J. 373 (2019) 624–641.

[27]H. Derikvandi, A. Nezamzadeh-Ejhieh, J. Colloid Interface Sci. 490 (2017) 314–327.

[28]A. Nezamzadeh-Ejhieh, H. Zabihi-Mobarakeh, J. Ind. Eng. Chem. 20 (2014) 1421–1431.

[29]N.T. Sahrin, R. Nawaz, F.K. Chong, S.L. Lee, M.D.H. Wirzal, Environ. Technol. Innov. 22 (2021) 101418.

[30]T. Wang, Y. Li, W.-T. Wu, Y. Zhang, L. Wu, H. Chen, Appl. Surf. Sci. 537 (2021) 148025.

[31]S. Abdelnasser, R. Al Sakkaf, G. Palmisano, J. Environ. Chem. Eng. 9 (2021) 104873.

[32]H. Derikvandi, A. Nezamzadeh-Ejhieh, J. Hazard. Mater. 321 (2017) 629–638.

[33]M. Arunkumar, A.S. Nesaraj, Iran. J. Catal. 10 (2020) 235–245.

[34]A. Rostami-Vartooni, A. Moradi-Saadatmand, M. Bagherzadeh, Iran. J. Catal. 9 (2018) 27–35.

[35]M. Babaahamdi-Milani, A. Nezamzadeh-Ejhieh, J. Hazard. Mater. 318 (2016) 291–301.

[36]A. Rahmani-Aliabadi, A. Nezamzadeh-Ejhieh, J. Photochem. Photobiol. Chem. 357 (2018) 1–10.

[37]H. Derikvandi, A. Nezamzadeh-Ejhieh, Solid State Sci. 101 (2020) 106127.

[38]N. Omrani, A. Nezamzadeh-Ejhieh, J. Photochem. Photobiol. Chem. 389 (2020) 112223.

[39]J. Esmaili-Hafshejani, A. Nezamzadeh-Ejhieh, J. Hazard. Mater. 316 (2016) 194–203.

[40]S.A. Mirsalari, A. Nezamzadeh-Ejhieh, Sep. Purif. Technol. 250 (2020) 117235.

[41]S. Azimi, A. Nezamzadeh-Ejhieh, J. Mol. Catal. Chem. 408 (2015) 152–160.

[42]A.N. Ejhieh, M. Khorsandi, J. Hazard. Mater. 176 (2010) 629–637.

[43]F. Soleimani, A. Nezamzadeh-Ejhieh, J. Mater. Res. Technol. 9 (2020) 16237–16251.

[44]H. Derikvandi, M. Vosough, A. Nezamzadeh-Ejhieh, Int. J. Hydrog. Energy 46 (2021) 2049–2064.

[45]T.-F. Yeh, J.-M. Syu, C. Cheng, T.-H. Chang, H. Teng, Adv. Funct. Mater. 20 (2010) 2255–2262.

[46]D.J. Martin, G. Liu, S.J.A. Moniz, Y. Bi, A.M. Beale, J. Ye, J. Tang, Chem. Soc. Rev. 44 (2015) 7808–7828.

[47]W.S. Koe, J.W. Lee, W.C. Chong, Y.L. Pang, L.C. Sim, Environ. Sci. Pollut. Res. 27 (2020) 2522–2565.

[48]S. Gupta, M. Tripathi, Open Chem. 10 (2012) 279-284.

[49]C. Chen, W. Ma, J. Zhao, Chem. Soc. Rev. 39 (2010) 4206-4219.

[50]V. Etacheri, C. Di Valentin, J. Schneider, D. Bahnemann, S.C. Pillai, J. Photochem. Photobiol. C Photochem. Rev. 25 (2015) 1–29.

[51]J. Maragatha, S. Rajendran, T. Endo, S. Karuppuchamy, J. Mater. Sci. Mater. Electron. 28 (2017) 5281–5287.

[52]N.T. Tung, D.N. Huyen, J. Nanomater. 2016 (2016) 1–7.

[53]R.S. Dariani, A. Esmaeili, A. Mortezaali, S. Dehghanpour, Optik 127 (2016) 7143–7154.

[54]S. Challagulla, R. Nagarjuna, R. Ganesan, S. Roy, Nano-Struct. Nano-Objects 12 (2017) 147–156.

[55]L. Spadaro, F. Arena, A. Palella, in: Photocatalytic Reduct. CO2 New Chall. Sol. Energy Exploit., Elsevier, 2018, 429–472.

[56]K. Pathakoti, S. Morrow, C. Han, M. Pelaez, X. He, D.D. Dionysiou, H.-M. Hwang, Environ. Sci. Technol. 47 (2013) 9988–9996.

[57]H. Zabihi-Mobarakeh, A. Nezamzadeh-Ejhieh, J. Ind. Eng. Chem. 26 (2015) 315–321.

[58]A. Nezamzadeh-Ejhieh, M. Bahrami, Desalination Water Treat. 55 (2015) 1096–1104.

[59]M. Balakrishnan, R. John, Iran. J. Catal. 10 (2020) 235–245.

[60]A. Besharati-Seidani, Iran. J. Catal. 6 (2016) 447–454.

[61]S. Dianat, Iran. J. Catal. 8 (2018) 121–132.

[62]N.E. Fard, R. Fazaeli, Iran. J. Catal. 8 (2018) 133–141.

[63]B. Khodadadi, Iran. J. Catal. 6 (2016) 305–311.

[64]A. Mahmoodi, S.M. Mehdinia, A. Rahmani, H. Nassehinia, Iran. J. Catal. 10 (2020) 23–32.

[65]J.T. Mehrabad, M. Partovi, F.A. Rad, R. Khalilnezhad, Iran. J. Catal. 9 (2018) 233–239.

[66]H.F. Moafi, Iran. J. Catal. 6 (2016) 281–292.

[67]H.R. Pouretedal, M. Fallahgar, F.S. Pourhasan, M. Nasiri, Iran. J. Catal. 7 (2017) 317–326.

[68]T. Seyedi-Chokanlou, S. Aghabeygi, N. Molahasani, F. Abrinaei, Iran. J. Catal. 11 (2021) 49–58.

[69]J. Prakash, Samriti, A. Kumar, H. Dai, B.C. Janegitz, V. Krishnan, H.C. Swart, S. Sun, Mater. Today Sustain. 13 (2021) 100066.

[70]D. Awfa, M. Ateia, M. Fujii, M.S. Johnson, C. Yoshimura, Water Res. 142 (2018) 26–45.

[71]M. Nemiwal, T.C. Zhang, D. Kumar, Sci. Total Environ. 767 (2021) 144896.

[72]S.M. Patil, S.A. Vanalakar, S.A. Sankpal, S.P. Deshmukh, S.D. Delekar, Results Chem. 3 (2021) 100102.

[73]J.C. Durán-Álvarez, V.A. Hernández-Morales, M. Rodríguez-Varela, D. Guerrero-Araque, D. Ramirez-Ortega, F. Castillón, P. Acevedo-Peña, R. Zanella, Catal. Today 341 (2020) 71–81.

[74]M.A. Behnajady, H. Eskandarloo, J. Nanosci. Nanotechnol. 13 (2013) 548–553.

[75]S. Hoang, S. Guo, C.B. Mullins, J. Phys. Chem. C 116 (2012) 23283–23290.

[76]W. Xie, R. Li, Q. Xu, Sci. Rep. 8 (2018) 8752.

[77]C. Hao, W. Wang, R. Zhang, B. Zou, H. Shi, Sol. Energy Mater. Sol. Cells 174 (2018) 132–139.

[78]J.S. Khaw, M. Curioni, P. Skeldon, C.R. Bowen, S.H. Cartmell, J. Nanotechnol. 2019 (2019) 1–13.

[79]J.-Y. Park, K.-I. Choi, J.-H. Lee, C.-H. Hwang, D.-Y. Choi, J.-W. Lee, Mater. Lett. 97 (2013) 64–66.

[80]A. Mayabadi, A. Pawbake, S. Rondiya, A. Rokade, R. Waykar, R. Kulkarni, A. Jadhavar, M. Kamble, B. Gabhale, V. Waman, V. Sathe, H. Pathan, S. Jadkar, Thin Solid Films 589 (2015) 493–502.

[81]Z. He, Q. Cai, H. Fang, G. Situ, J. Qiu, S. Song, J. Chen, J. Environ. Sci. 25 (2013) 2460–2468.

[82]Y.-Z. Chen, R.-J. Wu, L.-Y. Lin, W.-C. Chang, J. Power Sources 413 (2019) 384–390.

[83] D. T, V.R. K., V. M., B. K., C. B., R.R. K., Appl. Surf. Sci. 435 (2018) 216–224.

[84] W. Zhang, S. Chen, S. Yu, Y. Yin, J. Cryst. Growth 308 (2007) 122–129.

[85] J. Zhang, P. Zhou, J. Liu, J. Yu, Phys Chem Chem Phys 16 (2014) 20382–20386.

[86] P. Bouras, E. Stathatos, P. Lianos, Appl. Catal. B Environ. 73 (2007) 51–59.

[87] K. Fischer, A. Gawel, D. Rosen, M. Krause, A. Abdul Latif, J. Griebel, A. Prager, A. Schulze, Catalysts 7 (2017) 209.

[88] M. Monai, T. Montini, P. Fornasiero, Catalysts 7 (2017) 304.

[89] W. Hu, L. Li, G. Li, C. Tang, L. Sun, Cryst. Growth Des. 9 (2009) 3676–3682.

[90] Z. Li, S. Cong, Y. Xu, ACS Catal. 4 (2014) 3273–3280.

[91] R. Daghrir, P. Drogui, D. Robert, Ind. Eng. Chem. Res. 52 (2013) 3581–3599.

[92] L.V. Bora, R.K. Mewada, Renew. Sustain. Energy Rev. 76 (2017) 1393–1421.

[93] M.R.D. Khaki, M.S. Shafeeyan, A.A.A. Raman, W.M.A.W. Daud, J. Environ. Manage. 198 (2017) 78–94.

[94] C. Liao, Y. Li, S.C. Tjong, Nanomaterials 10 (2020) 124.

[95] S. Mousavi-Mortazavi, A. Nezamzadeh-Ejhieh, Desalination Water Treat. 57 (2016) 10802–10814.

[96] X. Zhao, G. Zhang, Z. Zhang, Environ. Int. 136 (2020) 105453.

[97] S.I. Mogal, M. Mishra, V.G. Gandhi, R.J. Tayade, Mater. Sci. Forum 734 (2012) 364–378.

[98] Q. Zhang, Appl. Catal. B Environ. 26 (2000) 207–215.

[99] W. Zhang, Y. Chen, S. Yu, S. Chen, Y. Yin, Thin Solid Films 516 (2008) 4690–4694.

[100] N. Omrani, A. Nezamzadeh-Ejhieh, Sep. Purif. Technol. 235 (2020) 116228.

[101] M.I. Litter, in: P. Boule, D.W. Bahnemann, P.K.J. Robertson (Eds.), Environ. Photochem. Part II, Springer-Verlag, Berlin/Heidelberg, 2005, 325–366.

[102] R. Leary, A. Westwood, Carbon 49 (2011) 741–772.

[103] M.D. Hernández-Alonso, F. Fresno, S. Suárez, J.M. Coronado, Energy Environ. Sci. 2 (2009) 1231-1257.

[104] M. Mehrali-Afjani, A. Nezamzadeh-Ejhieh, H. Aghaei, Chem. Phys. Lett. 759 (2020) 137873.

[105] N. Omrani, A. Nezamzadeh-Ejhieh, J. Photochem. Photobiol. Chem. 400 (2020) 112726.

[106] N. Raeisi-Kheirabadi, A. Nezamzadeh-Ejhieh, Int. J. Hydrog. Energy 45 (2020) 33381–33395.

[107] S.A. Mirsalari, A. Nezamzadeh-Ejhieh, Mater. Sci. Semicond. Process. 122 (2021) 105455.

[108] P. Bezerra, R. Cavalcante, A. Garcia, H. Wender, M. Martines, G. Casagrande, J. Giménez, P. Marco, S. Oliveira, A. Machulek Jr., J. Braz. Chem. Soc. 28 (9) (2017) 1788-1802.

[109] H.A. Foster, I.B. Ditta, S. Varghese, A. Steele, Appl. Microbiol. Biotechnol. 90 (2011) 1847–1868.

[110] Y. Cho, W. Choi, J. Photochem. Photobiol. Chem. 148 (2002) 129–135.

[111] T.S. Natarajan, H.C. Bajaj, R.J. Tayade, J. Colloid Interface Sci. 433 (2014) 104–114.

[112] J. Fang, F. Shi, J. Bu, J. Ding, S. Xu, J. Bao, Y. Ma, Z. Jiang, W. Zhang, C. Gao, W. Huang, J. Phys. Chem. C 114 (2010) 7940–7948.

[113] S.I. Mogal, V.G. Gandhi, M. Mishra, S. Tripathi, T. Shripathi, P.A. Joshi, D.O. Shah, Ind. Eng. Chem. Res. 53 (2014) 5749–5758.

[114] S. Ghattavi, A. Nezamzadeh-Ejhieh, J. Mol. Liq. 322 (2021) 114563.

[115] S. Ghattavi, A. Nezamzadeh-Ejhieh, DESALINATION WATER Treat. 166 (2019) 92–104.

[116] S. Ghattavi, A. Nezamzadeh-Ejhieh, Compos. Part B Eng. 183 (2020) 107712.

[117] S. Ghattavi, A. Nezamzadeh-Ejhieh, Int. J. Hydrog. Energy 45 (2020) 24636–24656.

[118] R. Bacsa, J. Kiwi, T. Ohno, P. Albers, V. Nadtochenko, J. Phys. Chem. B 109 (2005) 5994–6003.

[119] E. Moctezuma, B. Zermeño, E. Zarazua, L.M. Torres-Martínez, R. García, Top. Catal. 54 (2011) 496–503.

[120] J. Choi, H. Park, M.R. Hoffmann, J. Phys. Chem. C 114 (2010) 783–792.

[121] M. Nasirian, C.F. Bustillo-Lecompte, M. Mehrvar, J. Environ. Manage. 196 (2017) 487–498.

[122] L.M. Santos, W.A. Machado, M.D. França, K.A. Borges, R.M. Paniago, A.O.T. Patrocinio, A.E.H. Machado, RSC Adv. 5 (2015) 103752–103759.

[123] A. Norouzi, A. Nezamzadeh-Ejhieh, Phys. B Condens. Matter 599 (2020) 412422.

[124] A.B. Ghomi, V. Ashayeri, Iran. J. Catal. 2 (2012) 135–140.

[125] S.D. Khairnar, M.R. Patil, V.S. Shrivastava, Iran. J. Catal. 8 (2018) 143–150.

[126] M.M.J. Sadiq, A.S. Nesaraj, Iran. J. Catal. 4 (2014) 219–226.

[127] M. Samandari, A.T. Manesh, S.A. Hosseini, S. Mansouri, Iran. J. Catal. 11 (2021) 175–180.

[128] A. Sobhani-Nasab, M. Eghbali-Arani, S.M. Hosseinpour-Mashkani, F. Ahmadi, M. Rahimi-Nasrabadi, V. Ameri, Iran. J. Catal. 10 (2018) 91–99.

[129] S. Jafari, A. Nezamzadeh-Ejhieh, J. Colloid Interface Sci. 490 (2017) 478–487.

[130] R.P. Cavalcante, R.F. Dantas, B. Bayarri, O. González, J. Giménez, S. Esplugas, A. Machulek, Catal. Today 252 (2015) 27–34.

[131] L. Gao, W. Gan, S. Xiao, X. Zhan, J. Li, RSC Adv. 5 (2015) 52985–52992.

[132] H. Derikvandi, A. Nezamzadeh-Ejhieh, J. Mol. Catal. Chem. 426 (2017) 158–169.

[133] M. Sankarammal, A. Thatheyus, D. Ramya, Open J. Water Pollut. Treat. 2014 (2014) 92–100.

[134] M. Fashola, V. Ngole-Jeme, O. Babalola, Int. J. Environ. Res. Public. Health 13 (2016) 1047.

[135] C. Cervantes, J. Campos-García, S. Devars, F. Gutiérrez-Corona, H. Loza-Tavera, J.C. Torres-Guzmán, R. Moreno-Sánchez, FEMS Microbiol. Rev. 25 (2001) 335–347.

[136] A. Malik, Environ. Int. 30 (2004) 261–278.

[137] A. Fathima, J.R. Rao, Arch. Microbiol. 200 (2018) 453–462.

[138] R. Kumar, D. Bhatia, R. Singh, S. Rani, N.R. Bishnoi, Int. Biodeterior. Biodegrad. 65 (2011) 1133–1139.

[139] N.S. Kumaran, A. Sundaramanicam, S. Bragadeeswaran, J. Appl. Sci. Res. 7 (2011) 1609–1615.

[140] A. Bhattacharya, A. Gupta, Environ. Sci. Pollut. Res. 20 (2013) 6628–6637.

[141] S.A. Jafari, S. Cheraghi, M. Mirbakhsh, R. Mirza, A. Maryamabadi, CLEAN - Soil Air Water 43 (2015) 118–126.

[142] S.M. Al-Garni, K.M. Ghanem, A.S. Ibrahim, Afr. J. Biotechnol. 9 (2010) 6413–6421.

[143] A.H. Caravelli, L. Giannuzzi, N.E. Zaritzky, J. Hazard. Mater. 156 (2008) 214–222.

[144] S. Murugavelh, K. Mohanty, Environ. Eng. Manag. J. 13 (2014) 281–287.

[145] S. Zhang, S.A. Crow, Appl. Environ. Microbiol. 67 (2001) 4030–4035.

[146] B Thippeswamy, C K Shivakumar, M Krishnappa, PubMed 33 (2012) 1063–1068.

[147] P.C. Mane, A.B. Bhosle, Int. J. Environ. Res. 6 (2012)571-576.

[148] W. Zhang, B. Xiong, L. Chen, K. Lin, X. Cui, H. Bi, M. Guo, W. Wang, Environ. Toxicol. Pharmacol. 36 (2013) 51–57.

[149] L. Regaldo, S. Gervasio, H. Troiani, A.M. Gagneten, J. Algal Biomass Util. 4 (2013) 59–66.

[150] R. Fagan, D.E. McCormack, D.D. Dionysiou, S.C. Pillai, Mater. Sci. Semicond. Process. 42 (2016) 2–14.

[151] I. Paspaltsis, K. Kotta, R. Lagoudaki, N. Grigoriadis, I. Poulios, T. Sklaviadis, J. Gen. Virol. 87 (2006) 3125–3130.

[152] R. Nakano, M. Hara, H. Ishiguro, Y. Yao, T. Ochiai, K. Nakata, T. Murakami, J. Kajioka, K. Sunada, K. Hashimoto, A. Fujishima, Y. Kubota, Catalysts 3 (2013) 310–323.

[153] D.J. Giannantonio, J.C. Kurth, K.E. Kurtis, P.A. Sobecky, Int. Biodeterior. 8 (2009) 252-259.

[154] M. Sökmen, S. Değerli, A. Aslan, Exp. Parasitol. 119 (2008) 44–48.

[155] E. Ruiz-Hitzky, M. Darder, B. Wicklein, C. Ruiz-Garcia, R. Martín-Sampedro, G. del Real, P. Aranda, Adv. Healthc. Mater. 9 (2020) 2000979.

[156] H. Choi, M.G. Antoniou, M. Pelaez, Environ. Sci. Technol. 41 (2007) 7530-7535.

[157] X. He, A. Wang, P. Wu, S. Tang, Y. Zhang, L. Li, P. Ding, Sci. Total Environ. 743 (2020) 140694.

[158] J. Ananpattarachai, Y. Boonto, P. Kajitvichyanukul, Environ. Sci. Pollut. Res. 23 (2016) 4111–4119.

[159] Y. Wang, Y. Wu, H. Yang, X. Xue, Z. Liu, Vacuum 131 (2016) 58–64.

[160] N.K. Eswar, P.C. Ramamurthy, G. Madras, New J. Chem. 40 (2016) 3464–3475.

[161] T. Feng, J. Liang, Z. Ma, M. Li, M. Tong, Colloids Surf. B Biointerfaces 167 (2018) 275–283.

[162] C.-K. Huang, T. Wu, C.-W. Huang, C.-Y. Lai, M.-Y. Wu, Y.-W. Lin, Appl. Surf. Sci. 399 (2017) 10–19.

[163] J. Liang, F. Liu, J. Deng, M. Li, M. Tong, Water Res. 123 (2017) 632–641.

[164] J. Xu, Z. Wang, Y. Zhu, ACS Appl. Mater. Interfaces 9 (2017) 27727–27735.

[165] W. Bing, Z. Chen, H. Sun, P. Shi, N. Gao, J. Ren, X. Qu, Nano Res. 8 (2015) 1648–1658.

[166] Y. Li, Y. Li, S. Ma, P. Wang, Q. Hou, J. Han, S. Zhan, J. Hazard. Mater. 338 (2017) 33–46.

[167] N.S. Ahmad, N. Abdullah, F. Yasin, Bioresource 4 (2019) 8866–8878.

[168] K.-P. Yu, Y.-T. Huang, S.-C. Yang, J. Hazard. Mater. 261 (2013) 155–162.

[169] M. Miyauchi, K. Sunada, K. Hashimoto, Catalysts 10 (2020) 1093.

[170] P.-C. Maness, S. Smolinski, D.M. Blake, Z. Huang, E.J. Wolfrum, W.A. Jacoby, Appl. Environ. Microbiol. 65 (1999) 4094–4098.

[171] C. Guillard, T.-H. Bui, C. Felix, V. Moules, B. Lina, P. Lejeune, Comptes Rendus Chim. 11 (2008) 107–113.

[172] H. Takashima, Y. Iida, K. Nakamura, Y. Kanno, in: 2006 IEEE Int. Conf. Syst. Man Cybern., IEEE, Taipei, Taiwan, 2006, pp. 1413–1418.

[173] Y. Kikuchi, K. Sunada, T. Iyoda, K. Hashimoto, A. Fujishima, J. Photochem. Photobiol. Chem. 106 (1997) 51–56.

[174] C. Hu, J. Guo, J. Qu, X. Hu, Langmuir 23 (2007) 4982–4987.

[175] T. Saito, T. Iwase, J. Horie, T. Morioka, J. Photochem. Photobiol. B 14 (1992) 369–379.

[176] W. Kangwansupamonkon, V. Lauruengtana, S. Surassmo, U. Ruktanonchai, Nanomedicine Nanotechnol. Biol. Med. 5 (2009) 240–249.

[177] K. Sunada, T. Watanabe, K. Hashimoto, J. Photochem. Photobiol. Chem. 156 (2003) 227–233.

[178] K. Sunada, Y. Kikuchi, K. Hashimoto, A. Fujishima, Environ. Sci. Technol. 32 (1998) 726–728.

[179] M. Suwalsky, C. Schneider, H.D. Mansilla, J. Kiwi, J. Photochem. Photobiol. B 78 (2005) 253–258.

[180] J. Kiwi, V. Nadtochenko, J. Phys. Chem. B 108 (2004) 17675–17684.

[181] V. Nadtochenko, N. Denisov, O. Sarkisov, D. Gumy, C. Pulgarin, J. Kiwi, J. Photochem. Photobiol. Chem. 181 (2006) 401–407.

[182] J. Kiwi, V. Nadtochenko, Langmuir 21 (2005) 4631–4641.

[183] J. Hou, L. Wang, C. Wang, S. Zhang, H. Liu, S. Li, X. Wang, J. Environ. Sci. 75 (2019) 40–53.

[184] Y. Chen, D.D. Dionysiou, Appl. Catal. B Environ. 62 (2006) 255–264.

[185] K.-J. Hwang, J.-W. Lee, W.-G. Shim, H.D. Jang, S.-I. Lee, S.-J. Yoo, Adv. Powder Technol. 23 (2012) 414–418.

[186] O.O. Kelyp, I.S. Petrik, V.S. Vorobets, N.P. Smirnova, V.S. G.Ya. Kolbasov, Chem. Phys. Surf. Technol. 4 (2015) 105–112.

[187] Y. Chen, A. Lin, F. Gan, Powder Technol. 167 (2006) 109–116.

[188] X. Zhang, X. Li, J. Wu, R. Yang, L. Tian, Z. Zhang, J. Sol-Gel Sci. Technol. 51 (2009) 1–3.

[189] R. Nandanwar, P. Singh, F.Z. Haque, Int. J. Chem. Phys. Sci. 3 (2014) 40–45.

[190]W. Nachit, S. Touhtouh, Z. Ramzi, M. Zbair, A. Eddiai, M. Rguiti, A. Bouchikhi, A. Hajjaji, K. Benkhouja, Mol. Cryst. Liq. Cryst. 627 (2016) 170–175.

[191]Z. Adriana, Recent Pat. Eng. 2 (2008) 157–164.

[192]A. Zielińska, E. Kowalska, J.W. Sobczak, I. Łącka, M. Gazda, B. Ohtani, J. Hupka, A. Zaleska, Sep. Purif. Technol. 72 (2010) 309–318.

[193]S. Esposito, Materials 12 (2019) 668.

[194]S.A. Yazid, Z.M. Rosli, J.M. Juoi, J. Mater. Res. Technol. 8 (2019) 1434–1439.

[195]C. Guillard, B. Beaugiraud, C. Dutriez, J.-M. Herrmann, H. Jaffrezic, N. Jaffrezic-Renault, M. Lacroix, Appl. Catal. B Environ. 39 (2002) 331–342.

[196]S.M. Lam, J.C. Sin, A.R. Mohamed, Recent Pat. Chem. Eng. 1 (2010) 209–219.

[197]A. Zyoud, A. Zu'bi, M.H.S. Helal, D. Park, G. Campet, H.S. Hilal, J. Environ. Health Sci. Eng. 13 (2015) 46.

[198]L. Hu, T. Yoko, H. Kozuka, S. Sakka, Thin Solid Films 219 (1992) 18–23.

[199]Y. Zhu, L. Zhang, C. Gao, L. Cao, J. Mater. Sci. 35 (2000) 4049–4054.

[200]I. El Saliby, Y. Okour, H.K. Shon, J. Kandasamy, W.E. Lee, J.-H. Kim, J. Ind. Eng. Chem. 18 (2012) 1033–1038.

[201]V. Štengl, S. Bakardjieva, J. Bludská, J. Mater. Sci. 46 (2011) 3523–3536.

[202]F. Chen, X. Yang, Q. Wu, Build. Environ. 44 (2009) 1088–1093.

[203]T. Ohno, K. Sarukawa, K. Tokieda, M. Matsumura, J. Catal. 203 (2001) 82–86.

[204]V. Štengl, V. Houšková, N. Murafa, S. Bakardjieva, Ceram. – Silikáty 54 (2010) 368–378.

[205]H. Mehranpour, M. Askari, M.S. Ghamsari, H. Farzalibeik, J. Nanomater. 2010 (2010) 1–5.

[206]D. Ganguli, Bull. Mater. Sci. 15 (1992) 421–430.

[207]S. Basu, P. Bhattacharyya, Sens. Lett. 9 (2011) 1575–1591.

[208]D.-S. Seo, J.-K. Lee, H. Kim, J. Cryst. Growth 229 (2001) 428–432.

[209]P.J. Kelly, R.D. Arnell, Vacuum 56 (2000) 159–172.

[210]X. Fu, S. Qutubuddin, Colloids Surf. Physicochem. Eng. Asp. 179 (2001) 65–70.

[211]G. Fu, P.S. Vary, C.-T. Lin, J. Phys. Chem. B 109 (2005) 8889–8898.

[212]R. Najjar, M. Shokri, S. Farsadi, Desalination Water Treat. 54 (2015) 2581–2591.

[213]Y. Wang, H. Cheng, Y. Hao, J. Ma, W. Li, S. Cai, Thin Solid Films 349 (1999) 120–125.

[214]A.M. Tripathi, R.G. Nair, S.K. Samdarshi, Sol. Energy Mater. Sol. Cells 94 (2010) 2379–2385.

[215]F. Wu, X. Li, Z. Wang, C. Xu, H. He, A. Qi, X. Yin, H. Guo, Hydrometallurgy 140 (2013) 82–88.

[216]T.S. Mackey, J. Met. 46 (1994) 59–64.

[217]T.A.I. Lasheen, Hydrometallurgy 76 (2005) 123–129.

[218]R. Razavi, S. Hosseini, M. Ranjbar, Iran. J. Chem. Chem. Eng 33 (2014) 29–36.

[219]R.K. Biswas, M.G.K. Mondal, Hydrometallurgy 17 (1987) 385–390.

[220]Z. Li, Z. Wang, G. Li, Powder Technol. 287 (2016) 256–263.

[221]E.M. Mahdi, M.H. Abdul Shukor, Y.M.S. Meor, P. Wilfred, J. Nano Res. 21 (2012) 71–76.

[222]D. Wibowo, Int. J. ChemTech Res. 9 (2016) 483-491.

[223]M.R. Lanyon, T. Lwin, R.R. Merritt, Hydrometallurgy 51 (1999) 299–323.

[224]W. Jonglertjunya, T. Rubcumintara, Asia-Pac. J. Chem. Eng. 8 (2013) 323–330.

[225]A.M. Amer, Hydrometallurgy 67 (2002) 125–133.

[226]F. Wu, X. Li, Z. Wang, L. Wu, H. Guo, X. Xiong, X. Zhang, X. Wang, Int. J. Miner. Process. 98 (2011) 106–112.

[227]L. Wu, X. Li, Z. Wang, H. Guo, X. Wang, F. Wu, J. Fang, Z. Wang, L. Li, J. Alloys Compd. 506 (2010) 271–278.

[228]X.-Y. Chuan, A.H. Lu, J. Chen, N. Li, Y.J. Guo, Mineral. Petrol. 93 (2008) 143–152.

[229]N.G. Kostova, M. Achimovičová, A. Eliyas, N. Velinov, V. Blaskov, I. Stambolova, E. Gock, Bulg. Chem. Commun. 47 (2015) 317–322.

[230]N.S. Rosli, C.A.C. Abdullah, R. Hazan, Results Phys. 11 (2018) 72–78.

[231]X. Wang, X. Li, Z. Wang, L. Wu, P. Yue, H. Guo, F. Wu, T. Ma, Powder Technol. 204 (2010) 198–202.

[232]T. Tao, Y. Chen, D. Zhou, H. Zhang, S. Liu, R. Amal, N. Sharma, A.M. Glushenkov, Chem. - Eur. J. 19 (2013) 1091–1096.

[233]Q.-H. Zhang, L. Gao, J.-K. Guo, Nanostructured Mater. 11 (1999) 1293–1300.

[234]J. Zhang, S. Yan, L. Fu, F. Wang, M. Yuan, G. Luo, Q. Xu, X. Wang, C. Li, Chin. J. Catal. 32 (2011) 983–991.

[235]S. Mourdikoudis, R.M. Pallares, N.T.K. Thanh, Nanoscale 10 (2018) 12871–12934.

[236]R. Nair, S. Paul, S.K. Samdarshi, Sol. Energy Mater. Sol. Cells 95 (2011) 1901–1907.

[237]M. Khairy, W. Zakaria, Egypt. J. Pet. 23 (2014) 419–426.

[238]N.D. Israelsen, C. Hanson, E. Vargis, Sci. World J. 2015 (2015) 1–12.

[239]A. Mattsson, L. Österlund, J. Phys. Chem. C 114 (2010) 14121–14132.

[240]Q. Yin, J. Xiang, X. Wang, X. Guo, T. Zhang, J. Exp. Nanosci. 11 (2016) 1127–1137.

[241]A. Mudhafar Mohammed, M. Sebek, C. Kreyenschulte, H. Lund, J. Rabeah, P. Langer, J. Strunk, N. Steinfeldt, J. Sol-Gel Sci. Technol. 91 (2019) 539–551.

[242]M. Ahamed, M.A.M. Khan, M.J. Akhtar, H.A. Alhadlaq, A. Alshamsan, Sci. Rep. 7 (2017) 17662.

[243]M. Chi, X. Sun, A. Sujan, Z. Davis, B.J. Tatarchuk, Fuel 238 (2019) 454–461.

[244]J.H. Lee, Y.S. Yang, J. Eur. Ceram. Soc. 25 (2005) 3573–3578.

[245]Y.-C. Lin, S.-H. Liu, H.-R. Syu, T.-H. Ho, Spectrochim. Acta. A. Mol. Biomol. Spectrosc. 95 (2012) 300–304.

[246]J. Chang, R.D. Taylor, R.A. Davidson, A. Sharmah, T. Guo, J. Phys. Chem. A 120 (2016) 2815–2823.

[247]C.P. Kumar, N.O. Gopal, T.C. Wang, M.-S. Wong, S.C. Ke, J. Phys. Chem. B 110 (2006) 5223–5229.

[248]Alamgir, W. Khan, S. Ahmad, N. Ahammed, A.H. Naqvi, in: Shimla, India, 2015, p. 080001.

[249]S. Wang, Y. Gao, Y. Qi, A. Li, F. Fan, C. Li, J. Catal. 354 (2017) 250–257.

[250]A. Miyoshi, J.J.M. Vequizo, S. Nishioka, Y. Kato, M. Yamamoto, S. Yamashita, T. Yokoi, A. Iwase, S. Nozawa, A. Yamakata, T. Yoshida, K. Kimoto, A. Kudo, K. Maeda, Sustain. Energy Fuels 2 (2018) 2025–2035.

[251]L. Sinatra, A.P. LaGrow, W. Peng, A.R. Kirmani, A. Amassian, H. Idriss, O.M. Bakr, J. Catal. 322 (2015) 109–117.

[252]D.S. Shinde, P.D. Bhange, S.S. Arbuj, J.-Y. Kim, J.-H. Bae, K.-W. Nam, S.N. Tayade, D.S. Bhange, Int. J. Hydrog. Energy 45 (2020) 8605–8617.

[253]Y.M. Hunge, M.A. Mahadik, A.V. Moholkar, C.H. Bhosale, Ultrason. Sonochem. 35 (2017) 233–242.

[254]P. Niu, G. Wu, P. Chen, H. Zheng, Q. Cao, H. Jiang, Front. Chem. 8 (2020) 172.

[255]N. Raghavan, S. Thangavel, Y. Sivalingam, G. Venugopal, Appl. Surf. Sci. 449 (2018) 712–718.

[256]M.S. Kumar, K.Y. Yasoda, D. Kumaresan, N.K. Kothurkar, S.K. Batabyal, Mater. Res. Express 5 (2018) 075502.

[257]M. Pawar, S. Topcu Sendoğdular, P. Gouma, J. Nanomater. 2018 (2018) 1–13.

[258]H. Chu, W. Lei, X. Liu, J. Li, W. Zheng, G. Zhu, C. Li, L. Pan, C. Sun, Appl. Catal. Gen. 521 (2016) 19–25.

[259]W. Sangchay, J. Nanotechnol. 2017 (2017) 1–7.

[260]M.F. La Russa, A. Macchia, S.A. Ruffolo, F. De Leo, M. Barberio, P. Barone, G.M. Crisci, C. Urzì, Int. Biodeterior. Biodegrad. 96 (2014) 87–96.

[261]G. Li, B. Wang, W.Q. Xu, Y. Han, Q. Sun, Dyes Pigments 155 (2018) 265–275.

[262]M.H.H. Mahmoud, A.A. Ismail, M.M.S. Sanad, Chem. Eng. J. 187 (2012) 96–103.

[263]Y.R. Smith, K. Joseph Antony Raj, V. (Ravi) Subramanian, B. Viswanathan, Colloids Surf. Physicochem. Eng. Asp. 367 (2010) 140–147.

[264]N.T. Lan, V.H. Anh, H.D. An, N.P. Hung, D.N. Nhiem, B. Van Thang, P.K. Lieu, D.Q. Khieu, J. Nanomater. 2020 (2020) 1–14.

[265]J.A. Torres-Luna, N.R. Sanabria, J.G. Carriazo, Powder Technol. 302 (2016) 254–260.

[266]S. Zhao, D. Kang, Z. Yang, Y. Huang, Appl. Surf. Sci. 488 (2019) 522–530.

[267]R.-B. Lee, J.-C. Juan, C.-W. Lai, K.-M. Lee, Chin. Chem. Lett. 28 (2017) 1613–1618.

[268]P. García-Muñoz, G. Pliego, J.A. Zazo, B. Barbero, A. Bahamonde, J.A. Casas, Chem. Eng. J. 318 (2017) 89–94.

[269]D. Xia, H. He, H. Liu, Y. Wang, Q. Zhang, Y. Li, A. Lu, C. He, P.K. Wong, Appl. Catal. B Environ. 238 (2018) 70–81.

[270]S. Kalantari, G. Emtiazi, J. Nanosci. Curr. Res. 01 (2016).